

old Version (left) and new version (right) comparison

Patterns of wintertime Arctic sea ice leads and their relation to winds and ocean currents

Sascha Willmes^{1,2}, Günther Heinemann², and Frank Schnaase³

¹Earth Observation and Climate Processes, Trier University

²Dpt. Environmental Meteorology, Trier, University

³Alfred Wegener Institute for Polar and Marine Research, Bremerhaven, Germany

Correspondence: Sascha Willmes (willmes@uni-trier.de)

Abstract. We use a novel sea-ice lead climatology based on satellite observations with 1 km² spatial resolution to identify predominant patterns in Arctic wintertime sea-ice leads. The causes for the observed spatial and temporal variabilities are investigated using ocean surface current velocities and eddy kinetic energies from an ocean model (FESOM) and winds from a regional climate model (CCLM) and ERA5 reanalysis, respectively. The presented investigation provides clear evidence for

5 the influence of ocean depth and associated currents on the mechanic weakening of sea ice and the accompanied occurrence of sea-ice leads with their characteristic spatial patterns. While the ocean influence on lead dynamics acts on a rather long-term scale (seasonal to inter-annual), the influence of wind appears to trigger sea-ice lead dynamics on shorter time scales of weeks to months and is largely controlled by individual events causing increased divergence.

1 Introduction

10 The fact that sea ice is mobile and exposed to ocean currents and winds causes it to be under constant tractions from above and below, which induces not only sea ice motion, but also internal stress and mechanical weakening. Therefore, sea ice exhibits a distinct dynamical character, which is mostly expressed through the formation of sea-ice leads in the divergent domain (e.g., Feltham, 2008). Knowledge about the variability and spatial distribution of leads is crucial as they promote a very strong exchange of heat and moisture between the relatively warm ocean and the cold winter atmosphere (Marcq and Weiss, 2012;

15 Lüpkes et al., 2008; Heinemann et al., 2022). Considering the observed changes in Arctic sea-ice extent and the projected trends, understanding the dynamics of leads is key to get a better insight into the feedbacks of the Arctic climate system (e.g. Wang et al., 2016; Zhang et al., 2012; Rheinlaender et al., 2022). Large-scale and high-resolution sea-ice deformation data are also important for improving short-term and seasonal sea-ice forecasts (Korosov et al., 2022; Nguyen et al., 2009). The potential of sea ice leads for preconditioning summer Arctic sea ice has been discussed (Zhang et al., 2018) and leads have

20 been recognized as a source of global methane, mercury and ozone emissions (Kort et al., 2012; Moore et al., 2014). The recurrence of leads and their spatial distribution are valuable diagnostic parameters for the sea-ice drift (e.g., Spreen et al., 2017; Kwok et al., 2013) and represent an essential habitat for marine mammals and birds (Stirling, 1997). Knowledge about the variability of sea-ice lead dynamics provides crucial information about the exchange of heat, the potential formation of new ice as well as the release of particles into the atmosphere (Creamean et al., 2022; Hartmann et al., 2022). Therefore,

Patterns of wintertime Arctic sea ice leads and their relation to winds and ocean currents

Sascha Willmes^{1,2}, Günther Heinemann², and Frank Schnaase³

¹Earth Observation and Climate Processes, Trier University

²Dpt. Environmental Meteorology, Trier, University

³Alfred Wegener Institute for Polar and Marine Research, Bremerhaven, Germany

Correspondence: Sascha Willmes (willmes@uni-trier.de)

Abstract. We use a novel sea-ice lead climatology for the winters of 2002/03 to 2020/21 based on satellite observations with 1 km² spatial resolution to identify predominant patterns in Arctic wintertime sea-ice leads. The causes for the observed spatial and temporal variabilities are investigated using ocean surface current velocities and eddy kinetic energies from an ocean model (FESOM) and winds from a regional climate model (CCLM) and ERA5 reanalysis, respectively. The presented investigation 5 provides evidence for the influence of ocean bathymetry and associated currents on the mechanic weakening of sea ice and the accompanied occurrence of sea-ice leads with their characteristic spatial patterns. The individual contribution of ocean and atmosphere to regional lead dynamics is, however, complex and a deeper insight requires detailed mechanistic investigations in combination with considerations of coastal geometries. While the ocean influence on lead dynamics seems to act on a rather long-term scale (seasonal to inter-annual), the influence of wind appears to trigger sea-ice lead dynamics on shorter time scales 10 of weeks to months and is largely controlled by individual events causing increased divergence. No significant pan-Arctic trends in wintertime leads can be observed. However, on the regional scale, months with both positive as well as with negative trends can be identified.

1 Introduction

The fact that sea ice is mobile and exposed to ocean currents and winds causes it to be under constant tractions from above and 15 below, which induces not only sea ice motion, but also internal stress and mechanical weakening. Therefore, sea ice exhibits a distinct dynamical character, which is mostly expressed through the formation of sea-ice leads in the divergent domain (e.g., Feltham, 2008). Knowledge about the variability and spatial distribution of leads is crucial as they promote a very strong exchange of heat and moisture between the relatively warm ocean and the cold winter atmosphere (Marcq and Weiss, 2012; Lüpkes et al., 2008; Heinemann et al., 2022). Considering the observed changes in Arctic sea-ice extent and the projected 20 trends, understanding the dynamics of leads is key to get a better insight into the feedbacks of the Arctic climate system (e.g. Wang et al., 2016; Zhang et al., 2012; Rheinlaender et al., 2022). Large-scale and high-resolution sea-ice deformation data are also important for improving short-term and seasonal sea-ice forecasts (Korosov et al., 2022; Nguyen et al., 2009). The potential of sea ice leads for preconditioning summer Arctic sea ice has been discussed (Zhang et al., 2018) and leads have been recognized as a source of global methane, mercury and ozone emissions (Kort et al., 2012; Moore et al., 2014). The

25 an identification and explanation of the factors that control sea-ice weakening and the associated lead patterns is key for a comprehensive understanding of air - sea ice – ocean interactions. Hence, especially in light of the observed trends in Arctic sea-ice extent (Stroeve and Notz, 2018), and with respect to the projected development of the Arctic climate system (Notz et al., 2020), the structure and dynamics of leads represent essential information for global change monitoring. While patterns in the spatial distribution of leads have recently been identified for both hemispheres with distinct spatial patterns (Reiser et 30 al., 2019; Willmes and Heinemann, 2016) the driving mechanisms for the profound variability in wintertime sea-ice dynamics are yet to be explained (e.g. Liu et al., 2022, Arthun et al., 2019; Hegyi and Taylor, 2017). The effect of warm air intrusions, extratropical atmospheric circulation and downward infrared radiation on the overall Arctic warming and sea-ice decline have been discussed (Warner et al., 2020; Park et al., 2015; Woods and Caballero, 2016) and first insights into the role of ocean currents on predominant lead occurrences, i.e. the Antarctic Slope Current in the Southern Ocean and the Arctic Boundary 35 Current, were given by Reiser et al., 2019 and Willmes and Heinemann, 2016, respectively.

In this paper we will first give an overview of the used data (Ch. 1) and then identify regions where leads are forming most frequently using a novel sea-ice lead climatology (Ch. 2). In Chapter 3, we show how predominant lead patterns in wintertime (Nov-Apr) Arctic sea ice as well as trends and anomalies have developed over the winters from 2002/2003 to 2020/2021 for different regions in the Arctic. Subsequently, we identify the influence of ocean floor topography and associated ocean currents 40 on spatial lead patterns by regional examples. Lastly, Chapter 3 shows how winds, especially the wind field divergence, has triggered temporal lead dynamics in some regions in the Arctic. The results are discussed in Chapter 4 before a comprehensive summary is given in Chapter 5.

2 Data and Methods

2.1 Sea-ice lead data

45 We use pan-Arctic daily binary lead maps from Moderate Resolution Imaging Spectroradiometer (MODIS) satellite infrared imagery at a resolution of 1 km² (data source: Reiser et al., 2020) to derive spatial and temporal lead patterns and a lead climatology for the Arctic Ocean. The daily grids contain one out of 4 basic categories per pixel and day including sea ice, clouds, artefacts and leads. The lead category indicates that the respective grid point was found to exhibit a significant positive surface temperature anomaly with respect to the surrounding sea-ice area in a kernel of 50x50 km². Artefacts can be considered 50 as an extension to the MODIS cloud mask as they represent a potential lead detection with, however, large retrieval uncertainty. The metrics and filtering mechanisms that apply to separate sea ice from leads and leads from artefacts, respectively, are described in detail in Reiser et al. (2020).

2.2 Bathymetry

To compare our data with ocean depth we use Version 4.0 of the International Bathymetric Chart of the Arctic Ocean (IBCAO) 55 Grid (Jakobsson et al., 2020). The data were acquired from gebco.net in Polar Stereographic projection co-ordinates (meters),

25 recurrence of leads and their spatial distribution are valuable diagnostic parameters for the sea-ice drift (e.g., Spreen et al., 2017; Kwok et al., 2013) and represent an essential habitat for marine mammals and birds (Stirling, 1997). Knowledge about the variability of sea-ice lead dynamics provides crucial information about the exchange of heat, the potential formation of new ice as well as the release of particles into the atmosphere (Creamean et al., 2022). Therefore, an identification and explanation of the factors that control sea-ice weakening and the associated lead patterns is key for a comprehensive understanding of air -
30 sea ice – ocean interactions. Hence, especially in light of the observed trends in Arctic sea-ice extent (Stroeve and Notz, 2018), and with respect to the projected development of the Arctic climate system (Notz et al., 2020), the structure and dynamics of leads represent essential information for monitoring Arctic climate change. Moreover, the younger and thinner ice that was observed during recent years is expected to be more prone to break-up and lead formation (Zhang et al., 2012). While patterns in the spatial distribution of leads have recently been identified for both hemispheres with distinct spatial patterns (Reiser et
35 al., 2019; Willmes and Heinemann, 2016) the driving mechanisms for the profound variability in wintertime sea-ice dynamics are yet to be explained (e.g. Liu et al., 2022, Arthun et al., 2019; Hegyi and Taylor, 2017). The effect of warm air intrusions, extratropical atmospheric circulation and downward infrared radiation on the overall Arctic warming and sea-ice decline have been discussed (Warner et al., 2020; Park et al., 2015; Woods and Caballero, 2016) and first insights into the role of ocean currents on predominant lead occurrences, i.e. the Antarctic Slope Current in the Southern Ocean and the Arctic Boundary
40 Current, were given by Reiser et al., 2019 and Willmes and Heinemann, 2016, respectively.

In this paper we will first give an overview of the used data (Ch. 2) and then identify regions where leads are forming most frequently using a novel sea-ice lead climatology (Ch. 3). In Chapter 3, we show how predominant lead patterns in wintertime (Nov-Apr) Arctic sea ice as well as trends and anomalies have developed over the winters from 2002/2003 to 2020/2021 for different regions in the Arctic. Subsequently, we identify the influence of ocean floor topography and associated ocean currents
45 on spatial lead patterns by regional examples. Lastly, Chapter 3 shows how winds, especially the wind field divergence, has triggered temporal lead dynamics in some regions in the Arctic. The results are discussed in Chapter 4 before a comprehensive summary is given in Chapter 5.

2 Data and Methods

2.1 Sea-ice lead data

50 We use pan-Arctic daily binary lead maps derived from Moderate Resolution Imaging Spectroradiometer (MODIS) satellite infrared imagery at a resolution of 1 km² (data source: <https://doi.org/10.1594/PANGAEA.955561>) to deduct spatial and temporal lead patterns and a lead climatology for the Arctic Ocean. The daily grids contain one out of 4 basic categories per pixel and day including sea ice, clouds, artefacts and leads. The lead category indicates that the respective grid point was found to exhibit a significant positive surface temperature anomaly with respect to the surrounding sea-ice area in a kernel of 50x50
55 km². This concept is based on the fact that during winter in leads the relatively warm ocean is exposed to a substantially colder atmosphere. Using this approach does not allow to distinguish between thin-ice and open water leads, but only accounts for the temperature anomaly. Artifacts can be considered as an extension to the MODIS cloud mask as they represent a potential lead

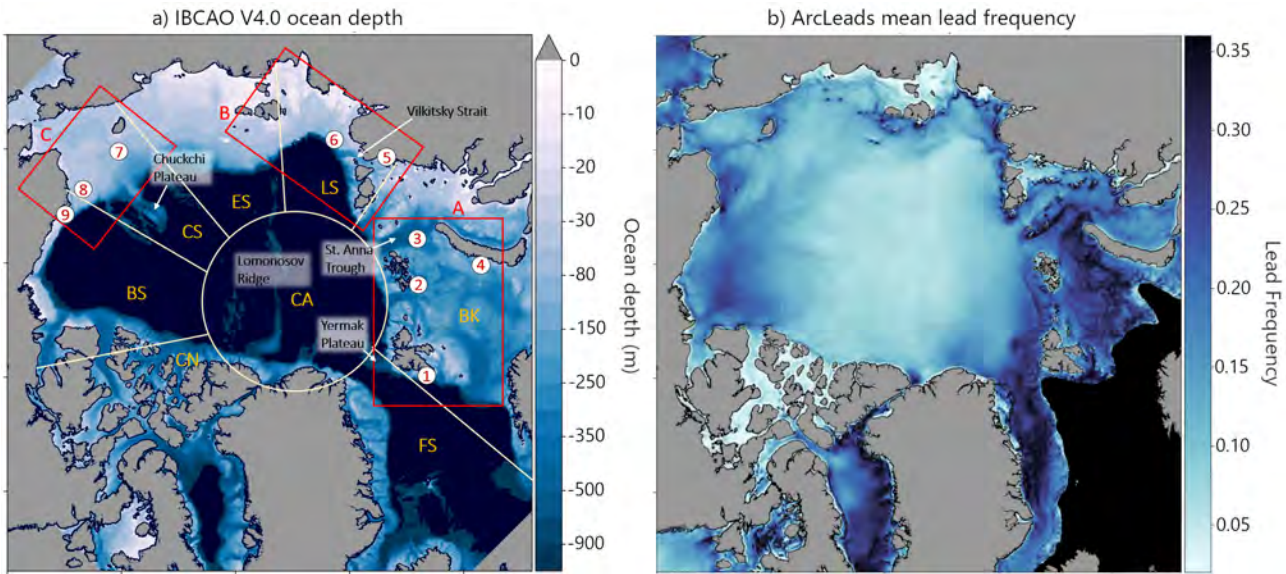


Figure 1. a) IBCAO V4.0 ocean depth (Jakobsson et al., 2020) and overview of the Arctic Ocean, analysed sub-regions and points of interest. Red boxes indicate regions used in Figures 3, 4 and 5., b) Pan-Arctic mean sea-ice lead frequencies for the months of NOV-APR in the period 2002/03 – 2020/21 (Reiser et al., 2020)

true scale set at 75°N. We re-projected the data to WGS 84 / NSIDC Sea Ice Polar Stereographic North (EPSG code: 3413) to match with our lead climatology.

2.3 Atmospheric data

Atmospheric data are taken from simulations of the non-hydrostatic regional climate model COnsortium for Small-scale MOdel 60 – Climate Limited area Mode (COSMO-CLM or CCLM, Steger and Buccignani, 2020). CCLM was adapted to polar regions by implementing a two-layer sea ice model and new parameterizations for the atmospheric boundary layer (Heinemann et al. 2021). CCLM has been used for several studies of air/sea-ice/ocean interactions and boundary layer processes in polar regions (e.g., Gutjahr et al. 2016; Kohnemann and Heinemann 2021, Heinemann et al. 2022). CCLM is used with a horizontal resolution of 15 km for the whole Arctic (C15). Initial and boundary data are taken from ERA-Interim reanalyses (Dee et al., 2011). The 65 model is used in a forecast mode with daily reinitialization. Model output is available every 1 h. Sea ice concentration is taken as daily data from AMSR2 data (Spreen et al., 2008). Sea ice thickness is prescribed daily from interpolated Pan-Arctic Ice Ocean Modeling and Assimilation System (PIOMAS) fields (Zhang und Rothrock, 2003). For the present study, monthly averages of wind field data at 10m are used. C15 data are available for the whole Arctic for 2002-2016. As a second atmospheric data set, we use ECMWF ERA5 data (Hersbach et al., 2020), which have a horizontal resolution of about 30 km. We here use monthly 70 averages of wind speed, horizontal wind components and wind divergence for the winter months November to April in the period 2002 to 2021 downloaded from the Copernicus Climate Data Store (<https://cds.climate.copernicus.eu/>).

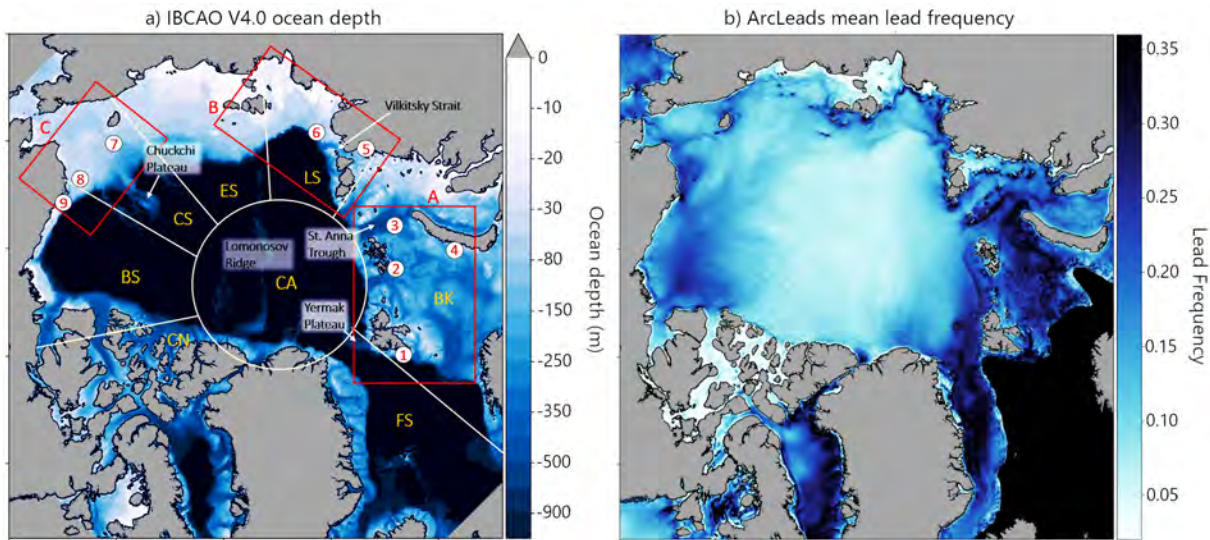


Figure 1. a) IBCAO V4.0 ocean depth (Jakobsson et al., 2020) and overview of the Arctic Ocean, analysed sub-regions and points of interest. Red boxes indicate regions used in Figures 3, 4 and 5., b) Pan-Arctic mean sea-ice lead frequencies for the months of NOV-APR in the period 2002/03 – 2020/21 (Reiser et al., 2020)

detection with, however, large retrieval uncertainty. The metrics and filtering mechanisms that apply to separate sea ice from leads and leads from artifacts, respectively, are described in detail in Reiser et al. (2020).

60 2.2 Bathymetry

To compare our data with ocean depth we use Version 4.0 of the International Bathymetric Chart of the Arctic Ocean (IBCAO) Grid (Jakobsson et al., 2020). The data were acquired from gebco.net in Polar Stereographic projection co-ordinates (meters), true scale set at 75°N. We re-projected the data to WGS 84 / NSIDC Sea Ice Polar Stereographic North (EPSG code: 3413) to match with our lead climatology.

65 2.3 Atmospheric data

Atmospheric data are taken from simulations of the non-hydrostatic regional climate model COnsortium for Small-scale MOdel – Climate Limited area Mode (COSMO-CLM or CCLM, Steger and Buccignani, 2020). CCLM was adapted to polar regions by implementing a two-layer sea ice model and new parameterizations for the atmospheric boundary layer (Heinemann et al. 2021). CCLM has been used for several studies of air/sea-ice/ocean interactions and boundary layer processes in polar regions (e.g., Gutjahr et al. 2016; Kohnemann and Heinemann 2021, Heinemann et al. 2022). CCLM is used with a horizontal resolution of 15 km for the whole Arctic (C15). Initial and boundary data are taken from ERA-Interim reanalyses (Dee et al., 2011). The model is used in a forecast mode with daily reinitialization. Model output is available every 1 h. Sea ice concentration is taken as daily data from AMSR2 data (Spreen et al., 2008). Sea ice thickness is prescribed daily from interpolated Pan-Arctic Ice Ocean

2.4 Ocean data

Ocean data of the surface current velocity (F_SCV) and Eddy Kinetic Energy (F_EKE) are from simulations of the Finite Elements Sea ice – ice-shelf – Ocean Model (FESOM) version 1.4 (Wang et al., 2014). FESOM was used in the same version as in Sidorenko et al. (2019), but with a different model grid. FESOM runs on a specialized grid with a global horizontal resolution of approximately 1°, which is refined to 4.5 km in the Arctic and 2 km for the Laptev Sea. Vertically it is structured into 47 layers with a resolution of 10 m in the upper 100 m and increased layer density near the bottom. Depth data is taken from the 1 minute version of the RTopo-2 dataset (Schaffer et al. 2016). The model is initialized with temperature and salinity data from the World Ocean Atlas (Levitus et al. 2013), river runoff is from the Japanese 55-year Reanalysis or JRA55 (Suzuki et al., 2018). On the global scale, FESOM is driven by ERA-Interim reanalyses (Dee et al. 2011) for the period 1987-2016. The model output is available as monthly means, with selected variables being available as daily means. We here use FESOM data for the Arctic for the period 2002-2016.

2.5 Data processing

Based on the method described in Reiser et al. (2020) and the resulting daily binary lead maps we calculate monthly lead frequencies as well the absolute mean lead frequency for the months of November to April for the winters of 2002/03 to 85 2015/16 (short period) and 2002/03 to 2020/21 (long period), respectively. The short period is used to allow for comparison with FESOM and C15 simulation results, which are available only up to April 2016. The long period is computed to make use of the full lead data set and allow comparisons with IBCAO ocean depth and ERA5 wind divergence. Two quantities are 90 calculated from the daily binary lead maps. The lead frequency (LFQ) is a temporally integrated quantity that indicates on how many days during a specified period a pixel is found to be covered by a lead, relative to number of the available clear-sky observations (Willmes and Heinemann, 2016). Thereby we obtain e.g., monthly, annual and total lead frequencies for the Arctic. Lead fraction area (LFA), in contrast, is a spatially integrated lead quantity that represents the fraction of a specified area that was covered by leads, i.e., the number of lead pixels over the sum of lead and sea ice pixels. If more than 50% of the given area are covered by clouds or artefacts (Reiser et al., 2020), the lead fraction is flagged “cloud covered”. The wind divergence 95 from C15 data was calculated from horizontal wind components at 10m. We also derived deformation and shear (Spreen et al., 2017) from the C15 wind data. Results for deformation and shear are, however, not shown here because no correlation was found between lead dynamics and these two parameters. For ERA5, we directly use the provided monthly divergence data for the 10m wind field. F_SCV is a direct model outputs of FESOM given as monthly averages. Monthly averaged Eddy Kinectic Energy (F_EKE) is calculated based on the monthly averaged surface velocities following Wekerle et al. (2017).

100 3 Results

Figure 1a provides an overview of the Arctic Ocean with IBCAO ocean depth and individual regions, sectors and points of interest for the subsequent description of detailed results and discussion. An overview of the spatial distribution of mean LFQ

Modeling and Assimilation System (PIOMAS) fields (Zhang und Rothrock, 2003). For the present study, monthly averages of 75 wind field data at 10m are used. C15 data are available for the whole Arctic for 2002-2016. As a second atmospheric data set, we use ECMWF ERA5 data (Hersbach et al., 2020), which have a horizontal resolution of about 30 km. We here use monthly averages of wind speed, horizontal wind components and wind divergence for the winter months November to April in the period 2002 to 2021 downloaded from the Copernicus Climate Data Store (<https://cds.climate.copernicus.eu/>).

2.4 Ocean data

80 Ocean data of the surface current velocity (F_SCV) and Eddy Kinetic Energy (F_EKE) are from simulations of the Finite Elements Sea ice – ice-shelf – Ocean Model (FESOM) version 1.4 (Wang et al., 2014). FESOM was used in the same version as in Sidorenko et al. (2019), but with a different model grid. FESOM runs on a specialized grid with a global horizontal resolution of approximately 1°, which is refined to 4.5 km in the Arctic and 2 km for the Laptev Sea. Vertically it is structured into 47 layers with a resolution of 10 m in the upper 100 m and increased layer density near the bottom. Depth data is taken 85 from the 1 minute version of the RTopo-2 dataset (Schaffer et al. 2016). The model is initialized with temperature and salinity data from the World Ocean Atlas (Levitus et al. 2013), river runoff is from the Japanese 55-year Reanalysis or JRA55 (Suzuki et al., 2018). On the global scale, FESOM is driven by ERA-Interim reanalyses (Dee et al. 2011) for the period 1987-2016. The model output is available as monthly means, with selected variables being available as daily means. We here use FESOM data for the Arctic for the period 2002-2016.

90 2.5 Data processing

Based on the method described in Reiser et al. (2020) and the resulting daily binary lead maps we calculate monthly lead frequencies as well the absolute mean lead frequency for the months of November to April for the winters of 2002/03 to 2015/16 (short period) and 2002/03 to 2020/21 (long period), respectively. The short period is used to allow for comparison with FESOM and C15 simulation results, which are available only up to April 2016. The long period is computed to make 95 use of the full lead data set and allow comparisons with ERA5 wind divergence. Two quantities are calculated from the daily binary lead maps. The lead frequency (LFQ) is a temporally integrated quantity that indicates on how many days during a specified period a pixel is found to be covered by a lead, relative to number of the available clear-sky observations (Willmes and Heinemann, 2016). Thereby we obtain e.g., monthly, annual and total lead frequencies for the Arctic. Lead fraction area (LFA), in contrast, is a spatially integrated lead quantity that represents the fraction of a specified area that was covered by 100 leads, i.e., the number of lead pixels over the sum of lead and sea ice pixels. If more than 50% of the given area are covered by clouds or artifacts (Reiser et al., 2020), the lead fraction is flagged “cloud covered”. The wind divergence from C15 data was calculated from horizontal wind components at 10m. We also derived shear and total deformation from the C15 wind data. These are, however, not shown here because no correlation was found between lead dynamics and these two parameters. For ERA5, we directly use the provided monthly divergence data for the 10m wind field. F_SCV is a direct model outputs 105 of FESOM given as monthly averages. Monthly averaged Eddy Kinetic Energy (F_EKE) is calculated based on the monthly averaged surface velocities following Wekerle et al. (2017).

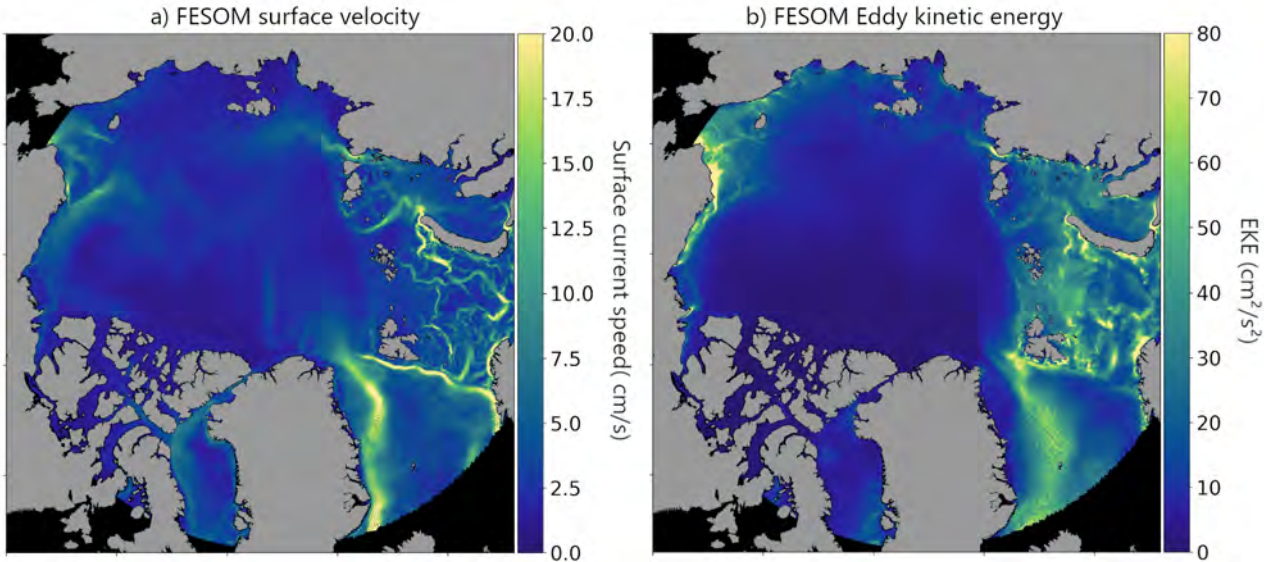


Figure 2. a) FESOM ocean surface current velocity (F_SCV) and b) FESOM eddy kinetic energies (F_EKE), NOV-APR, 2002/03 - 2015/2016.

based on the new lead climatology of Reiser et al. (2020) given in Figure 1b. There are several distinct spatial patterns in the observed lead climatology, which confirms the findings of Willmes and Heinemann (2016), but with far more detail. Increased 105 lead frequencies with values of up to 0.4 (pixel is covered by a lead in 40% of cases) are mainly found on the shelves, along the shelf break and alongside of channels and distinct bathymetric features (Fig. 1b). Several lead “hot spots” can be identified by darker shading that were hitherto unknown or at least not described in detail (see section 3.2). The most dominant spatial lead patterns are mainly found in Fram Strait (FS) and in the Barents / Kara Seas (BK), thus close to the marginal ice zone, where the ice pack becomes less dense due to the increased influence of ocean swell and waves (e.g. Bennetts et al., 2022). The lead 110 data shown here indicate, however, that also in the BK region we can spatially distinguish regions with pronounced LFQ that are associated with sea floor channels or ridges. Also, e.g., the northern edge of the Yermak plateau (northwest of Svalbard, Point 1 in Figure 1) shows an increased lead activity as compared to the surrounding, which gives rise to the assumption that mechanical or thermodynamical sea-ice weakening due to ocean currents influences sea-ice dynamics in this region. Similar patterns are also found around Franz-Josef Land (2), in St. Anna Trough (3) and west of Novaja Semlya (4). The Beaufort Sea 115 (BS) and its associated gyre are characterized by a significantly increased LFQ (>0.3) as compared to the central Arctic Ocean, where LFQ can drop down to below 0.05. The Laptev and East Siberian Seas (LS, ES) are mostly characterized by the extended fast-ice area and large flaw polynyas. Additionally, the shelf break as well as several small islands and shoals pop out in Fig. 1b with very high LFQ values (>0.4 in polynyas and over shoals). In the Chuckchi Sea (CS) we also find a distinct spatial pattern in the lead climatology that is obviously influenced by the sea floor. A first explanation of these findings is provided by 120 the results of FESOM simulations of ocean surface current velocities and EKE (Fig. 2a, b), showing that higher values in both

3 Results

Figure 1a provides an overview of the Arctic Ocean with IBCAO ocean depth and individual regions, sectors and points of interest for the subsequent description of detailed results and discussion. An overview of the spatial distribution of mean LFQ based on the new lead climatology of Reiser et al. (2020) given in Figure 1b. There are several distinct spatial patterns in the observed lead climatology, which confirms the findings of Willmes and Heinemann (2016), but with far more detail. Increased lead frequencies with values of up to 0.4 (pixel is covered by a lead in 40% of all days during winter) are mainly found on the shelves, along the shelf break and alongside of channels and distinct bathymetric features (Fig. 1b). Several lead “hot spots” can be identified by darker shading that were hitherto unknown or at least not described in detail (see section 3.2). The most dominant spatial lead patterns are mainly found in Fram Strait (FS) and in the Barents / Kara Seas (BK), thus close to the marginal ice zone, where the ice pack becomes less dense due to strong currents in combination with the increased influence of ocean swell and waves (e.g. Bennetts et al., 2022). The lead data shown here indicate, however, that also in the BK region we can spatially distinguish regions with pronounced LFQ that are associated with sea floor channels or ridges. Also, e.g., the northern edge of the Yermak plateau (northwest of Svalbard, Point 1 in Figure 1) shows an increased lead activity as compared to the surrounding, which gives rise to the assumption that mechanical or thermodynamical sea-ice weakening due to ocean current gradients and eddies (with the associated mixing) influences sea-ice dynamics in this region. Similar patterns are also found around Franz-Josef Land (2), in St. Anna Trough (3) and west of Novaja Semlya (4). The Beaufort Sea (BS) and its associated gyre are characterized by a significantly increased LFQ (values can exceed 0.3 in some regions) as compared to the central Arctic Ocean, where LFQ can drop down to below 0.05. The Laptev and East Siberian Seas (LS, ES) are mostly characterized by the extended fast-ice area and large flaw polynyas. Additionally, the shelf break as well as several small islands and shoals pop out in Fig. 1b with very high LFQ values (>0.4 in polynyas and over shoals). In the Chuckchi Sea (CS) we also find a distinct spatial pattern in the lead climatology that is obviously influenced by the sea floor.

3.1 Inter-annual and regional lead variability and trends

The MODIS lead climatology allows for an in-depth overview of wintertime sea-ice dynamics during the last two decades. As shown in Figure 2a, no overall trend is present in pan-Arctic monthly lead fractions (LFA). However, a significant seasonal and inter-annual variability can be noted with the tendency of a generally lower lead fraction at the end of winter (April) with frequency values of 0.1 on average compared to 0.15 in November. This is a reasonable finding considering the ice becoming thicker, more compact, and thus less mobile throughout the winter months. Subfigures 2b – 2i show the inter-annual and seasonal variability of lead fractions for individual regions (see map in Fig. 2a). None of the presented regions exhibits a significant trend. The magnitude of LFA differs between regions with the largest area covered by leads found in the FS sector (>0.5, note the different scales for individual regions). A strong seasonal variability is present in all regions, which is also indicated by the seasonal evolution of lead fractions per region (right panel for each region). While the change in area covered by leads is less pronounced in the FS, CN and BK sectors throughout winter, all other regions are characterized by a continuous decrease in lead fractions from November to April.

FESOM variables in many places occur with increased lead frequencies. This agreement is noteworthy especially because the two data sets are independent of one another (satellite data and simulation). The F_SCV clearly show what is usually referred to as the Arctic Boundary Current (Aksenov et al., 2011) with branches crossing the channels of the Barents Sea and entering the Siberian Sea via Vilkitsky Strait (5). Some of the spatial structures exhibited by these current branches resemble the lead patterns. For example, along the shelf break north of Svalbard, at the eastern edge of St. Anna Trough, in Vilkitsky Strait or in the Northern Chuckchi Sea, which gives rise to the hypothesis that ocean currents are an important driver for the mean susceptibility of sea ice lead occurrence. While increased current speeds are mostly associated with high F_EKE values the latter are more tied to bathymetric features and ocean depths above -1000 m.

3.1 Sea-ice leads, bathymetry and ocean currents

130 A more detailed perspective on the relation of lead frequencies, ocean depth and ocean currents is presented in Figures 3, 4 and 5 for three different sub-regions and transects.

3.1.1 Barents and Kara Seas

In Figure 3a, we show mean LFQ, IBCAO ocean depth, mean F_SCV and mean F_EKE in the Barents Sea (compare red rectangle around BK in Figure 1a). The spatial overview reveals the above-mentioned patterns in more detail. In many places 135 high LFQ values are associated with strong bathymetric gradients, increased current speeds and high F_EKE. Ocean depth in the Barents Sea ranges between -400 m and -100 m in the presented subset and is characterized by several elevations and channels with outlets towards the shelf break north of Svalbard (Point 1) and Franz-Josef Land (2), where ocean depth drops immediately to less than -1000 m. The eastern slope of St. Anna Trough (3) shows moreover a branch of significantly increased current speeds and a band of LFQ values above 0.4, which means that the sea ice in this region is covered by leads in more 140 than 40% of the time in the winter period from November to April. The highlighted transect (red) allows for a more detailed comparison in Figs. 3e and 3f. Reaching from northwest to southeast through the Barents Sea, the LFQ transect exhibits local maxima right above the indicated seafloor elevations, which reach from about -350 m up to -100 m in this region (Fig. 3e). At the northwestern coast of Novaya Zemlya the LFQ maximum is found over the slope rather than on top of the shelf (4). At this position the LFQ maximum is neighboured by strong maxima in F_SCV and F_EKE by the FESOM model (Fig. 3f). 145 The other seafloor elevations along the presented transect (e.g., at 69 km, 207 km, 345 km) are less accompanied by F_SCV or F_EKE maxima as by LFQ.

3.1.2 Laptev Sea

Similar features are found in a close-up for the Laptev Sea (Fig. 4, compare red rectangle around LS in Figure 1a). Most prominent here are the flaw polynyas and the extended fast ice area, which are characterized by high and low lead activity, 150 respectively. But increased LFQ values are also found in the outflow region of Vilkitsky Strait (5), between the Taimyr Peninsula and Bolshevik island, and along the shelf break (6). The chosen transect crosses Vilkitsky Strait up to the shelf and continues

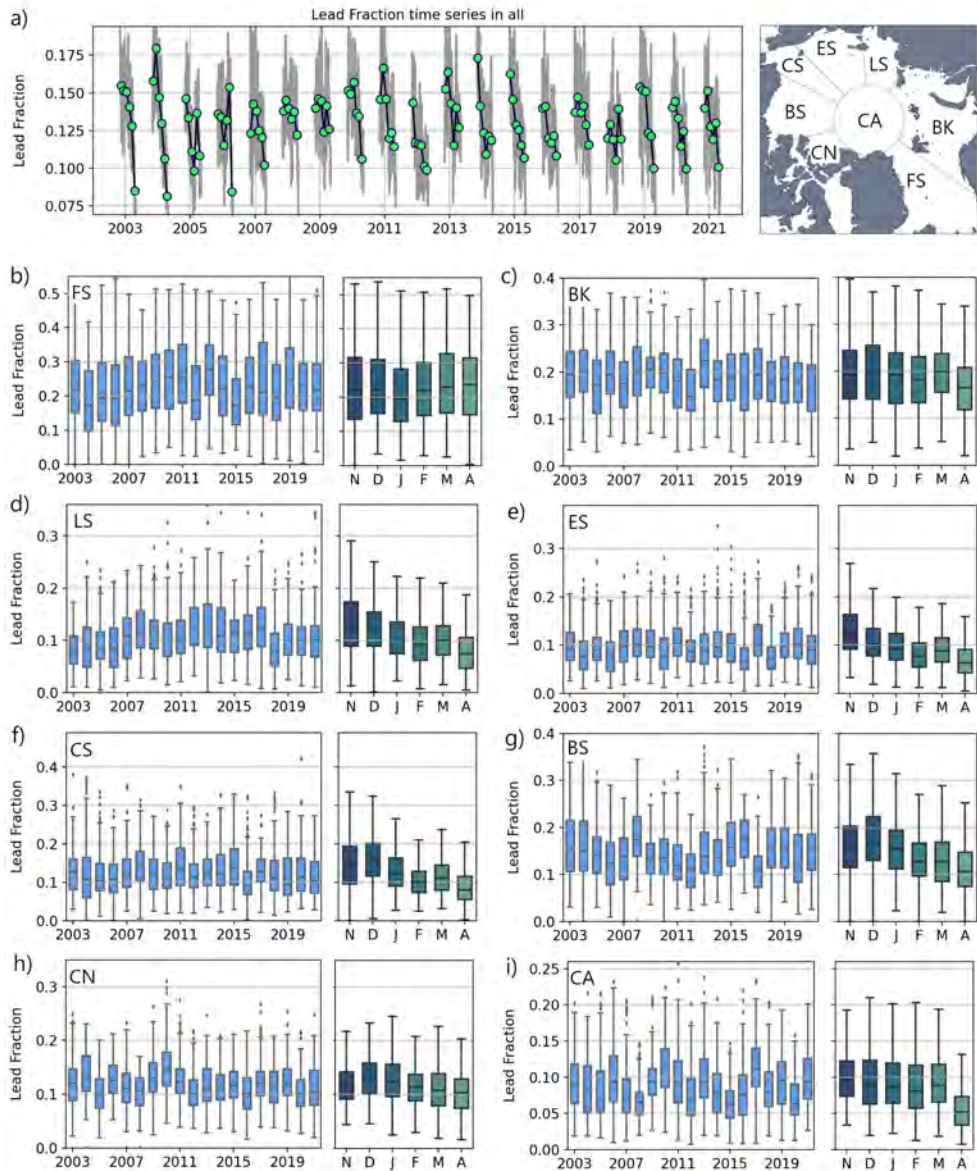


Figure 2. a) Time series of daily (grey) and monthly (green) Arctic lead fractions, all areas: Inset map indicates individual regions. b-f) Lead fractions for individual regions throughout years and months for regions indicated in inset map: Fram Strait (FS), Barents and Kara Seas (BK), Laptev Sea (LS), East Siberian Sea (ES), Chuckchi Sea (CS), Beaufort Sea (BS), Canadian Arctic (CN), Central Arctic (CA). The given spread per year represents the distribution of daily lead fractions per region and winter. Left panels: box-whisker plots for individual years with median, the 25% and 75% percentiles as the box, the 10% and 90% percentiles are plotted as error bars. Right panels: as left panels, but for individual months.

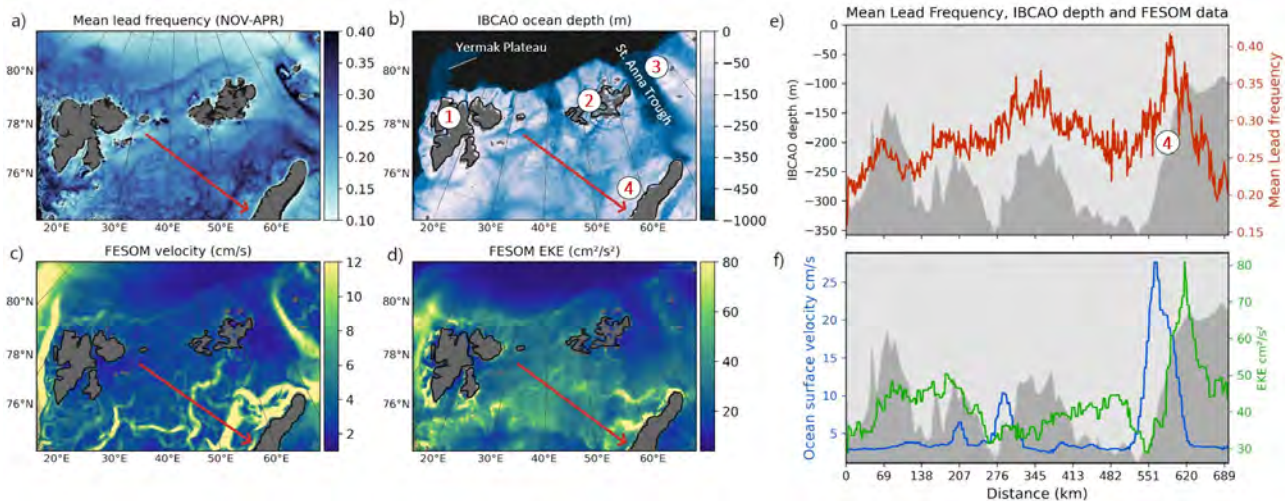


Figure 3. a) Mean wintertime lead frequency 2002-2016, b) IBCAO ocean depth (Jakobsson et al., 2020), c) mean FESOM surface current velocity (F_SCV) and d) mean FESOM EKE (F_EKE) in the Barents Sea; transect (red line) values: e) mean lead frequency (red) and ocean depth, f) FESOM current velocity (F_SCV, blue) and FESOM EKE (F_EKE, green), compare red box A in Figure 1a.

over the shelf break towards the deep ocean. Here, increased LFQ is found at the start of the transect southeast of Bolshevik Island where a flaw polynya is found, at the southern slope of Vilkitsky Trough and over the shelf break (Fig. 4e). Except from the flaw polynya, we find the mentioned LFQ maxima to be associated with maxima in both, F_SCV and F_EKE. Local

155 maxima for both parameters are found on the slope of Vilkitsky canyon as well as over the shelf break, indicating that the ocean plays a crucial role in shaping the sea ice stability in this region. The importance of the Vilkitsky canyon in transporting water masses was documented in several studies (e.g.: Harms and Karcher, 2005) with the general surface circulation in the Laptev Sea being characterized by an eastward flow that causes an inflow of saline water masses from Vilkitsky Strait (Janout et al. 2020). While the inflow itself does not explain increased lead frequencies in this region and over the shelf break, intensified 160 currents and tide-induced shear (Janout et al., 2015; Janout and Lenn, 2014) might be a driver for frequent sea-ice break-up. Thus, changing water masses and strong surface gradients in Vilkitsky Strait and over the Laptev Sea shelf break potentially represent favourable conditions for the formation of leads. The overall lead patterns in the Atlantic and Siberian sectors of the Arctic Ocean with increased lead frequencies over seafloor channels, ridges and along the shelf-break might therefore well be related to the structure and pathway of the Arctic Circumpolar Boundary Current (Pnyushkov et al., 2015, Aksenov et al., 165 2011).

3.1.3 Chuckchi Sea

In the Chuckchi Sea (Fig. 5, compare red rectangle around CS in Figure 1a) and around Wrangel Island we find some point-shaped areas of high LFQ and a linear band of slightly increased LFQ reaching from the north-eastern edge of Bering Strait towards Northwest. The IBCAO subset indicates that the latter pattern is associated with a shallow channel in this region,

140 In the central Arctic (CA) lead fractions are the lowest (<0.1 on average) and rather stable from November to March, but a significant drop is present from March to April, when lead fraction here is on average only around 0.05. Outliers in monthly lead fractions in all sectors indicate that strong anomalies are found only on the monthly scale, while there is no full year with extremely anomalous lead fractions on the pan-Arctic and on the regional scale. This finding is presented in more detail in latitude-averaged monthly LFQ anomalies in 5° longitude bins for Nov 2002 to April 2021.

145 Figure 3a shows the temporal evolution of LFQ anomalies in sea-ice regions between 70°N and 90°N across longitudes in the Arctic Ocean (the coastlines below the Figure indicate the respective position across longitudes). Significant trends are not identified. The most interesting feature here is an indication of strong lead events that are expressed through strong positive anomalies (red dots). Several of these events can be identified from the diagram across all longitudes while the Siberian sector of the Arctic (90°E - 180°E) is generally characterized by a variability that is less pronounced than in other sectors. Two events
150 are exemplarily extracted and shown as monthly lead anomaly maps.

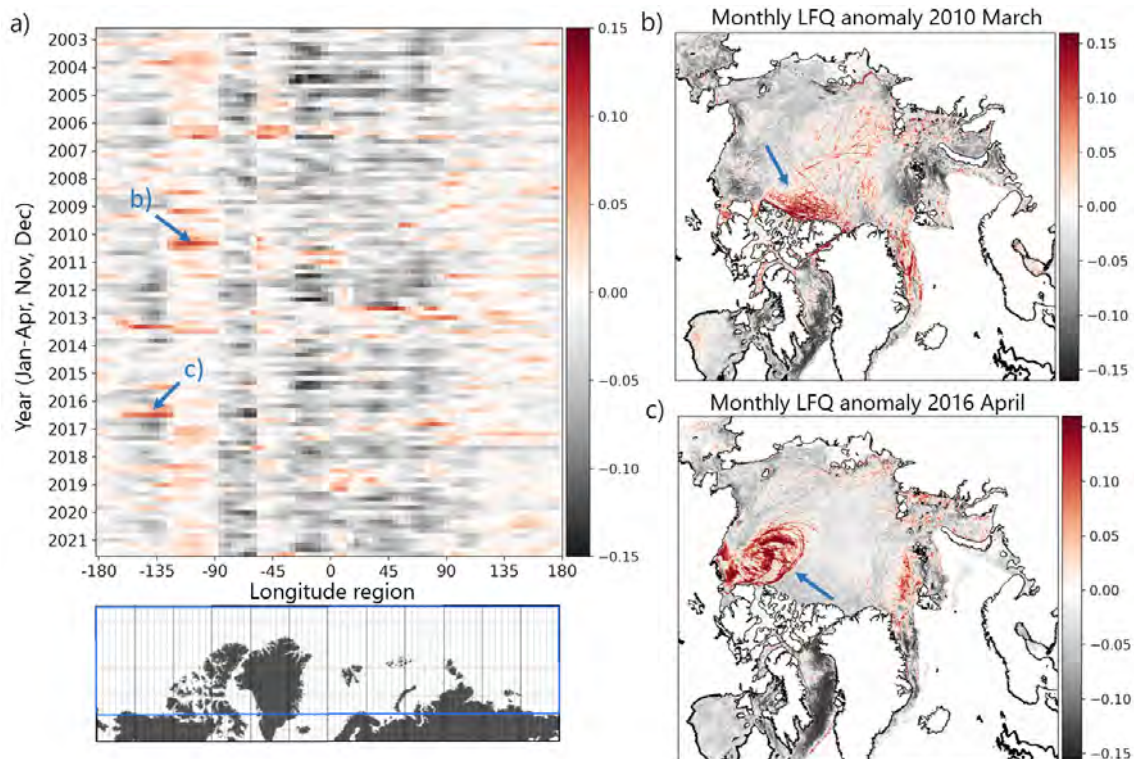


Figure 3. a) Latitude-averaged (70-90°N) monthly LFQ anomalies in 5° longitude bins for Nov 2002 to April 2021. Only the months Nov, Dec, Jan, Feb, Mar and Apr are shown, b) monthly lead frequency (LFQ) anomaly for 2010, Mar, with a very strong positive lead anomaly north of the Canadian Archipelago and c) monthly LFQ anomaly for 2016, April, underpinning the strong positive lead anomaly in the Beaufort Sea that is also given in the overview in a). Anomalies are calculated relative to the climatological monthly means.

In Figure 3b, the monthly LFQ map shows strong anomalies north of the Canadian Archipelago with values of up to 15% above average (see marker b for comparison in Fig. 3a). An extreme lead event in the Beaufort Sea in April 2016 with similar anomalies is shown in Figure 3c (marker c in Fig. 3a), which resulted from a series of preceding events that preconditioned the ice in the Beaufort Sea to become weaker and thinner (Babb et al., 2019). The event from 2013 in the Beaufort Sea discussed 155 in Rheinlaender et al. (2022) is also visible in Figure 3.

The question of trends in wintertime lead dynamics has been addressed in several studies so far. E.g., Wang et al. (2016) did not observe significant trends in the Arctic and Lewis and Hutchings (2019) did report no significant trend in the total number of days with leads per winter season. Qu et al. (2021) discuss a positive interannual trend in the April lead area of the Beaufort Sea and close relation to enhanced ice motion driven by an enhanced Beaufort High and persistent easterly winds.

160 Significant inter-annual trends cannot be found in our annual time series for this region (Figure 2g). However, we can confirm a significant trend in the April lead area fraction of the Beaufort Sea at 2% per decade ($p = 0.09$). On the monthly scale we find other significant positive trends, however with mostly small slopes, in the Laptev Sea in November (+2%/dec, $p=0.05$), in the Central Arctic in November (+1%/dec, $p=0.06$), in the East Siberian Sea in November (+1%/dec, $p=0.08$). But also significant negative trends are found: In the Barents and Kara Seas in March (-2%/dec, $p=0.09$), in the Beaufort Sea in February (-2%/dec, 165 $p=0.1$) and in the Canadian Arctic in January (-2%/dec, $p=0.03$) and February (-1%/dec, $p=0.08$).

3.2 Sea-ice leads, bathymetry and ocean currents

The mean spatial lead patterns presented in Figure 1b can be compared with FESOM simulations of ocean surface current velocities and EKE (Fig. 4a, b). One can see that higher values in both FESOM variables in many places occur with increased lead frequencies. This agreement is noteworthy especially because the two data sets are independent of one another (observations 170 and simulation). The F_SCV clearly show what is usually referred to as the Arctic Boundary Current (Aksenov et al., 2011) with branches crossing the channels of the Barents Sea and entering the Siberian Sea via Vilkitsky Strait (5). Some of the spatial structures exhibited by these current branches resemble the lead patterns. For example, along the shelf break north of Svalbard, at the eastern edge of St. Anna Trough, in Vilkitsky Strait or in the Northern Chuckchi Sea, which gives rise to the hypothesis that ocean currents are an important driver for the mean susceptibility of sea ice lead occurrence. While increased 175 current speeds are mostly associated with high F_EKE values the latter are more tied to bathymetric features and ocean depths above -1000 m.

A more detailed perspective on the relation of lead frequencies, ocean depth and ocean currents is presented in Figures 5, 6 and 7 for three different sub-regions and transects. These regions were selected because bathymetry is highly variable here a lot of details can be found in the patterns of LFQ, F_SCV and F_EKE.

180 3.2.1 Barents and Kara Seas

In Figure 5a, we show mean LFQ, IBCAO ocean depth, mean F_SCV and mean F_EKE in the Barents Sea (compare red rectangle around BK in Figure 1a). The spatial overview reveals the above-mentioned patterns in more detail. In many places high LFQ values are associated with strong bathymetric gradients, increased current speeds and high F_EKE. Ocean depth

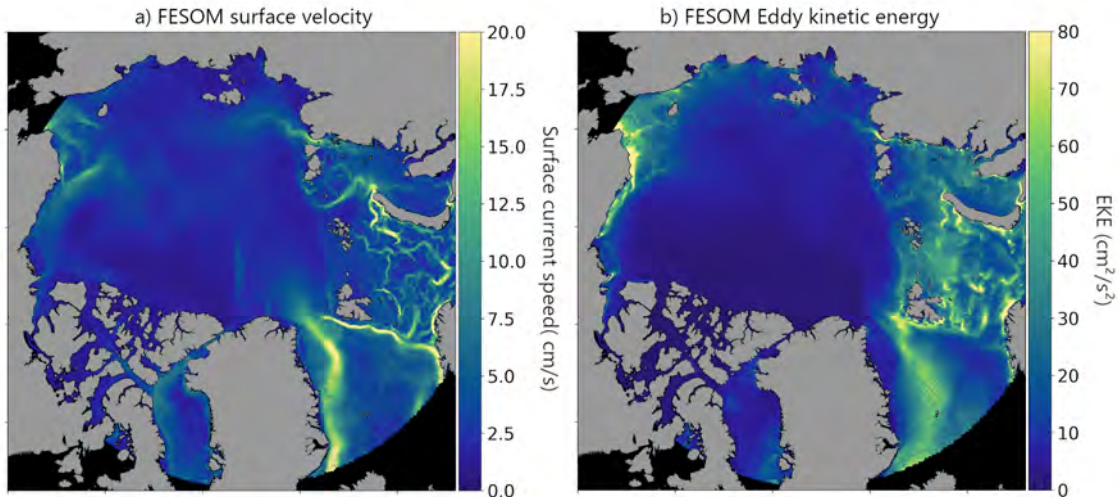


Figure 4. a) FESOM ocean surface current velocity (F_SCV) and b) FESOM eddy kinetic energy (F_EKE), NOV-APR, 2002/03 - 2015/2016.

in the Barents Sea ranges between -400 m and -100 m in the presented subset and is characterized by several elevations and channels with outlets towards the shelf break north of Svalbard (Point 1) and Franz-Josef Land (2), where ocean depth drops immediately to less than -1000 m. The eastern slope of St. Anna Trough (3) shows moreover a branch of significantly increased current speeds and a band of LFQ values above 0.4, which means that the sea ice in this region is covered by leads in more than 40% of the time in the winter period from November to April. The highlighted transect (red) allows for a more detailed comparison in Figs. 5e and 5f. Reaching from northwest to southeast through the Barents Sea, the LFQ transect exhibits local maxima right above the indicated seafloor elevations, which reach from about -350 m up to -100 m in this region (Fig. 5e). At the northwestern coast of Novaya Zemlya the LFQ maximum is found over the slope rather than on top of the shelf (4). At this position the LFQ maximum is neighboured by strong maxima in F_SCV and F_EKE by the FESOM model (Fig. 5f). The other seafloor elevations along the presented transect (e.g., at 69 km, 207 km, 345 km) are less accompanied by F_SCV or F_EKE maxima as by LFQ.

195 3.2.2 Laptev Sea

Similar features are found in a close-up for the Laptev Sea (Fig. 6, compare red rectangle around LS in Figure 1a). Most prominent here are the flaw polynyas and the extended fast ice area, which are characterized by high and low lead activity, respectively. But increased LFQ values are also found in the outflow region of Vilkitsky Strait (5), between the Taimyr Peninsula and Bolshevik island, and along the shelf break (6). The chosen transect crosses Vilkitsky Strait up to the shelf and continues 200 over the shelf break towards the deep ocean. Here, increased LFQ is found at the start of the transect southeast of Bolshevik Island where a flaw polynya is found, at the southern slope of Vilkitsky Trough and over the shelf break (Fig. 6e). Except from the flaw polynya, we find the mentioned LFQ maxima to be associated with maxima in both, F_SCV and F_EKE. Local

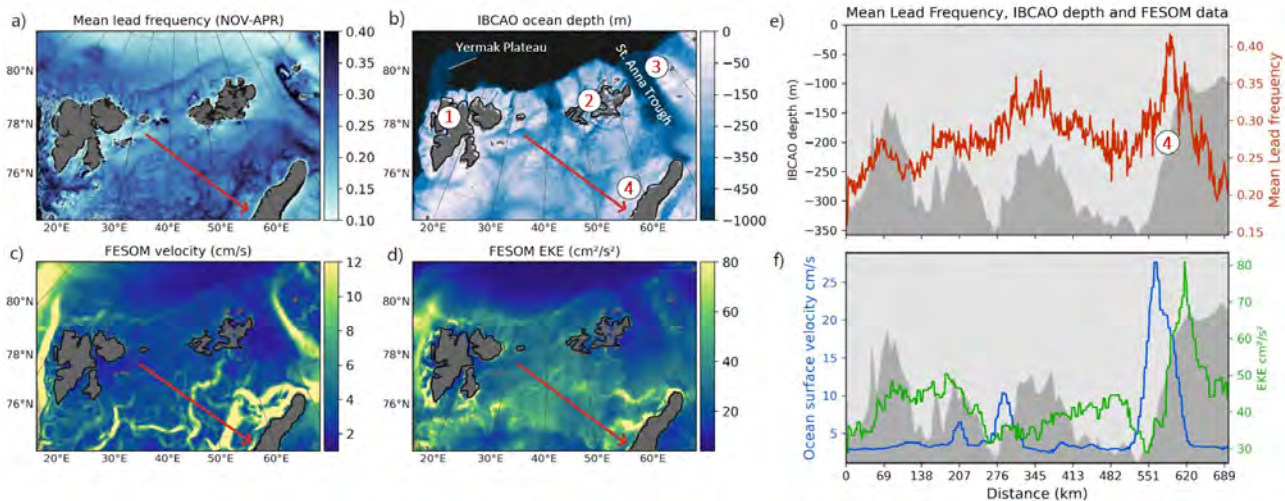


Figure 5. a) Mean wintertime lead frequency 2002-2016, b) IBCAO ocean depth (Jakobsson et al., 2020), c) mean FESOM surface current velocity (F_SCV) and d) mean FESOM EKE (F_EKE) in the Barents Sea; transect (red line) values: e) mean lead frequency (red) and ocean depth, f) FESOM current velocity (F_SCV, blue) and FESOM EKE (F_EKE, green), compare red box A in Figure 1a.

maxima for both parameters are found on the slope of Vilkitsky canyon as well as over the shelf break, indicating that the ocean plays a crucial role in shaping the sea ice stability in this region. The importance of the Vilkitsky canyon in transporting water masses was documented in several studies (e.g.: Harms and Kärcher, 2005) with the general surface circulation in the Laptev Sea being characterized by an eastward flow that causes an inflow of saline water masses from Vilkitsky Strait (Janout et al.

205 While the inflow itself does not explain increased lead frequencies in this region and over the shelf break, intensified currents and tide-induced shear (Janout et al., 2015; Janout and Lenn, 2014) might be a driver for frequent sea-ice break-up. Thus, changing water masses and strong surface gradients in Vilkitsky Strait and over the Laptev Sea shelf break potentially represent favourable conditions for the formation of leads. The overall lead patterns in the Atlantic and Siberian sectors of the 210 Arctic Ocean with increased lead frequencies over seafloor channels, ridges and along the shelf-break might therefore well be related to the structure and pathway of the Arctic Circumpolar Boundary Current (Pnyushkov et al., 2015, Aksenov et al, 2011).

3.2.3 Chuckchi Sea

215 In the Chuckchi Sea (Fig. 7, compare red rectangle around CS in Figure 1a) and around Wrangel Island we find some point-shaped areas of high LFQ and a linear band of slightly increased LFQ reaching from the north-eastern edge of Bering Strait towards Northwest. The IBCAO subset indicates that the latter pattern is associated with a shallow channel in this region,

i.e. Herald Canyon (7), and the southwestern slope of Herald Shoal (8), while the point-like LFQ maxima are found north 220 of Point Barrow (9), over Hanna Shoal (10) and next to a small island east of Wrangel. The ocean current velocities show two branches of increased speed reaching up north alongside of Herald Shoal. F_EKE values are increased next to the coast

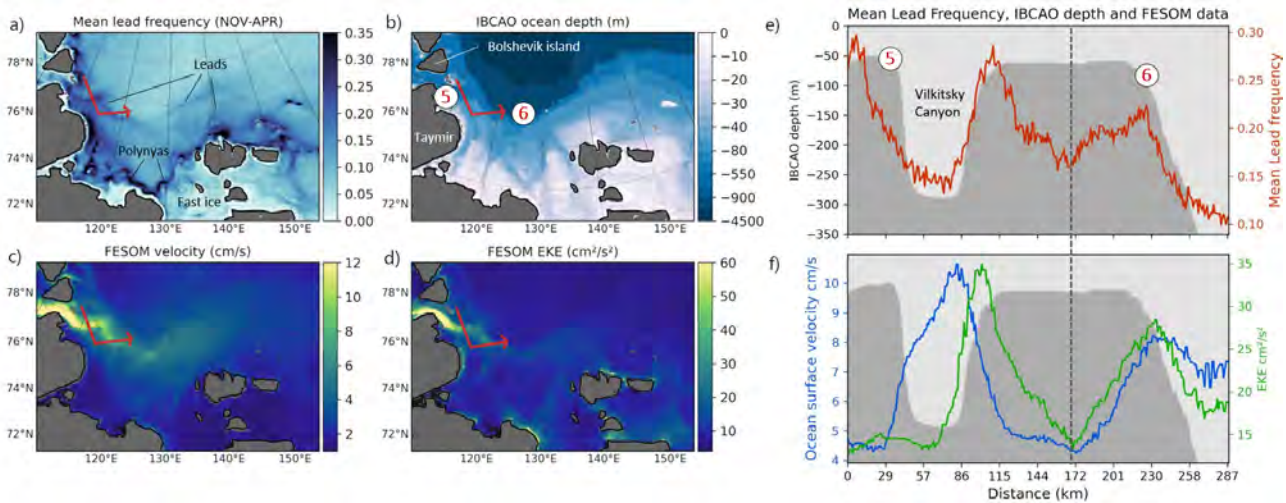


Figure 4. As in Figure 3 but for the Laptev Sea, compare red box B in Figure 1a.

170 i.e. Herald Canyon (7), and the southwestern slope of Herald Shoal (8), while the point-like LFQ maxima are found north
 of Point Barrow (9), over Hanna Shoal (10) and next to a small island east of Wrangel. The ocean current velocities show
 two branches of increased speed reaching up north alongside of Herald Shoal. F_EKE values are increased next to the coast
 and also in the band of increased LFQ on the western side of Herald Shoal. The profile in this subset crosses Herald Canyon,
 continues over Herald Shoal and ends in the central channel of the Chuckchi Sea. It indicates the strongly increased LFQ on
 175 the southwestern slope of Herald Shoal that is part of the band of higher LFQs mentioned above and with a pronounced peak
 right over Herald Shoal (Fig. 5e). The latter is accompanied by increased F_EKE in the ocean data, while the LFQ peak at the
 slope shows maxima for both, F_SCV and F_EKE (Fig. 5f). Towards the Central Channel, LFQ as well as F_SCV and F_EKE
 increase coincidentally. The indicated lead patterns can be attributed to the general circulation in the Chuckchi Sea, which is
 characterized by a broad northeasterly flow following the topography with some regions of intensified currents, e.g. in Herald
 180 Canyon (Winsor and Chapman, 2004; Stabeno et al., 2018).

3.1.4 Overall influence of surface currents and EKE

In order to pinpoint the Arctic regions, where the ocean (F_SCV and F_EKE) has the largest influence on the observed lead frequencies, we calculated what we refer to as the Conincident Percentile Exceedance (CPE), which is the percentile value that is exceeded in both data sets (LFQ and F_SCV or LFQ and F_EKE, respectively) at a certain position (Figure 6). This metric
 185 allows us to identify the regions, in which there is indication for the ocean to be as a significant driver for lead dynamics. The resulting map shows distinct patterns with CPE values over 90 in several regions (i.e. values are above the 90th percentile in both datasets). Most dominant are the Fram Strait, The Barents and Kara Seas, as well as the coast of Alaska, north of Point Barrow. Several bathymetric features can be recognized in both maps, e.g.: Herald Canyon in the Chuckchi Sea, the Vilkitsky

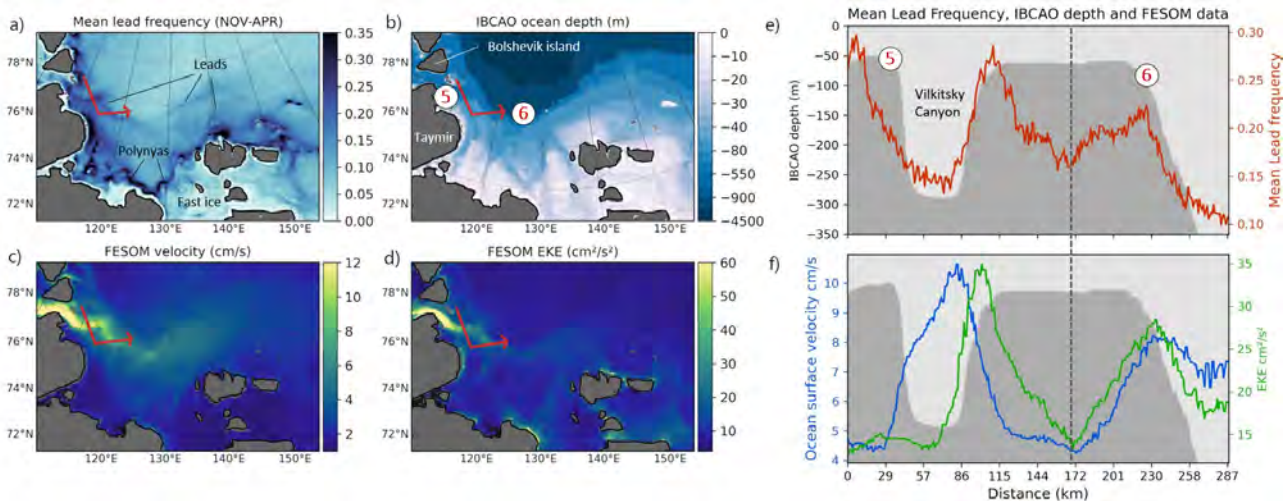


Figure 6. As in Figure 5 but for the Laptev Sea, compare red box B in Figure 1a.

and also in the band of increased LFQ on the western side of Herald Shoal. The profile in this subset crosses Herald Canyon, continues over Herald Shoal and ends in the central channel of the Chuckchi Sea. It indicates the strongly increased LFQ on the southwestern slope of Herald Shoal that is part of the band of higher LFQs mentioned above and with a pronounced peak right over Herald Shoal (Fig. 7e). The latter is accompanied by increased F_EKE in the ocean data, while the LFQ peak at the slope shows maxima for both, F_SCV and F_EKE (Fig. 7f). Towards the Central Channel, LFQ as well as F_SCV and F_EKE increase coincidentally. The indicated lead patterns can be attributed to the general circulation in the Chuckchi Sea, which is characterized by a broad northeasterly flow following the topography with some regions of intensified currents, e.g. in Herald Canyon (Winsor and Chapman, 2004; Stabeno et al., 2018).

3.2.4 Overall influence of surface currents and EKE

230 In order to pinpoint the Arctic regions, where the ocean (F_SCV and F_EKE) has the largest influence on the observed lead frequencies, we calculated what we refer to as the Conincident Percentile Exceedance (CPE), which is the percentile value that is exceeded in both data sets (LFQ and F_SCV or LFQ and F_EKE, respectively) at a certain position (Figure 8). This metric allows us to identify the regions, in which there is indication for the ocean to be a driver for lead dynamics. The resulting map shows distinct patterns with CPE values over 90 in several regions (i.e. values are above the 90% percentile in both datasets).

235 Most dominant are the Fram Strait, The Barents and Kara Seas, as well as the coast of Alaska, north of Point Barrow. Several bathymetric features can be recognized in both maps, e.g.: Herald Canyon in the Chuckchi Sea, the Vilkitsky Canyon in the western Laptev Sea or the slope of St. Anna Trough in the Kara Sea. In Fram Strait, we find high CPE for LFQ/F_SCV in a broad band between Greenland and Svalbard (Figure 8a), while the influence of F_EKE on leads seems to be limited to the marginal ice zone / ice edge in this region. In the Barents Sea we find individual current branches that are associated with high

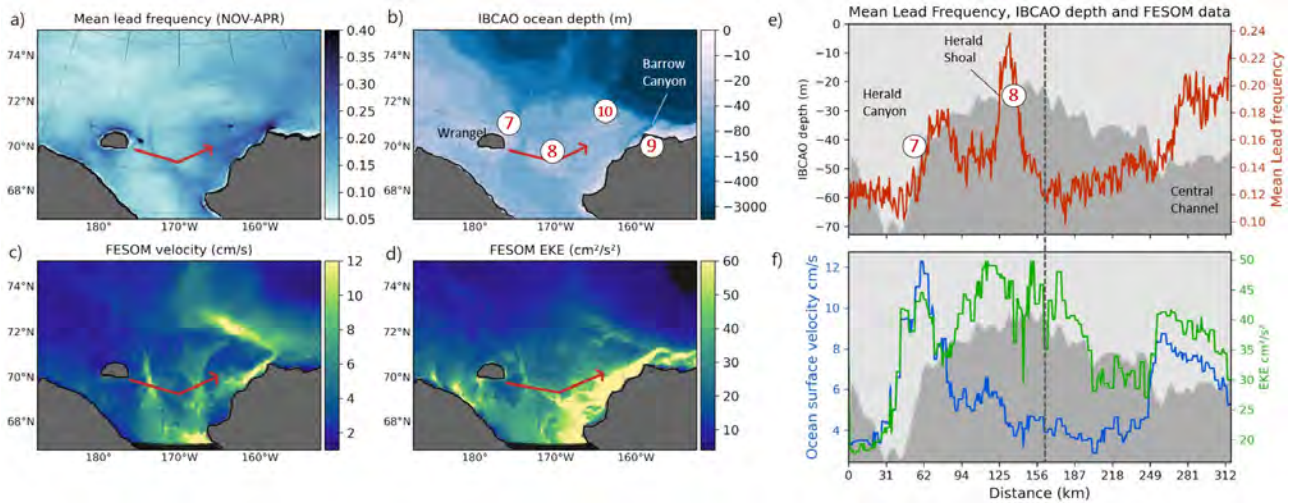


Figure 5. As in Figure 4 but for the Chuckchi Sea, compare red box C in Figure 1a.

Canyon in the western Laptev Sea or the slope of St. Anna Trough in the Kara Sea. In Fram Strait, we find high CPE for LFQ/F_SCV in a broad band between Greenland and Svalbard (Figure 6a), while the influence of F_EKE on leads seems to be limited to the marginal ice zone / ice edge in this region. In the Barents Sea we find individual current branches that are associated with high LFQ values. Many more interesting details can be seen in the two maps in Figure 6 that provide insight into how F_SCV and F_EKE affect the long-term lead dynamics individually and in which regions the stability of sea ice seems to be more prone to processes in the ocean.

195 3.1.5 Spatial lead patterns and winds

The presented results indicate that the effect of the ocean on sea-ice lead dynamics is most obvious in the long-term, that is, in the climatology. This is argued for by comparing IBCAO ocean depth with the mean fields of LFQ, F_SCV and F_EKE. As far as the atmosphere is concerned, average wind speed and shear (not shown) provide no indication of driving the observed patterns in the lead climatology. However, the mean wind divergence (Figure 7) shows a dominant region of positive divergence 200 centred around the Beaufort Gyre. This divergence pattern with maxima especially in the southern Beaufort Sea, is well aligned with the Beaufort Sea LFQ maximum indicated in Figure 1b. This broad region of generally increased lead occurrences might therefore be influenced by the mean divergence of the wind field rather than by ocean currents. Also, Fram Strait is characterized by a positive wind divergence in the long-term mean that can consequently add up to the influence of enhanced ocean currents 205 on average lead frequencies in this region. In general, however, winds seem to have a larger effect on the temporal dynamics of leads rather than on the mean spatial patterns. This will be presented in detail in section 3.3. First, however, an overview of the general spatio-temporal lead variability is presented.

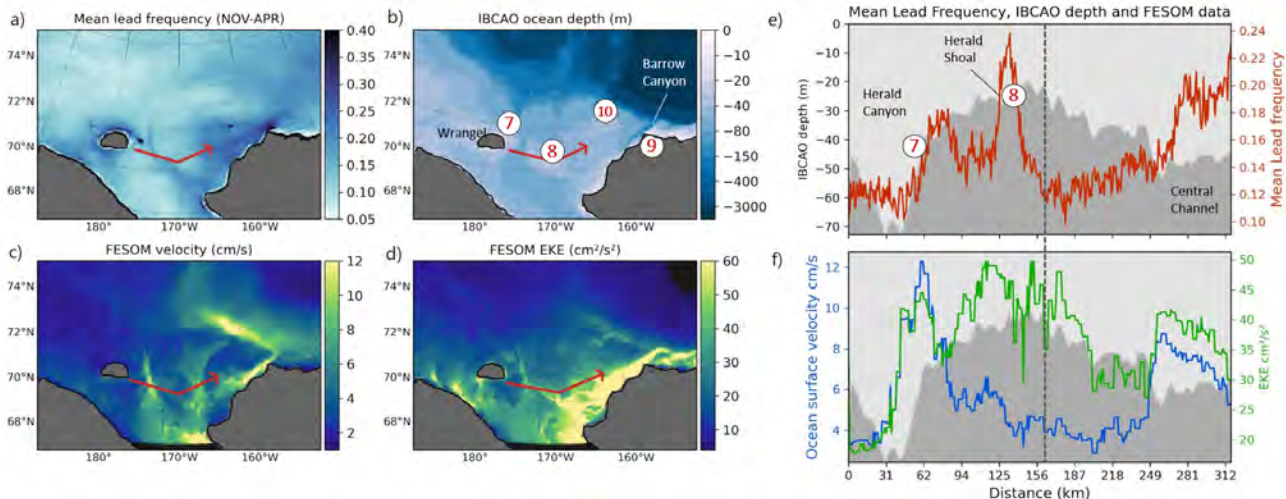


Figure 7. As in Figure 5 but for the Chuckchi Sea, compare red box C in Figure 1a.

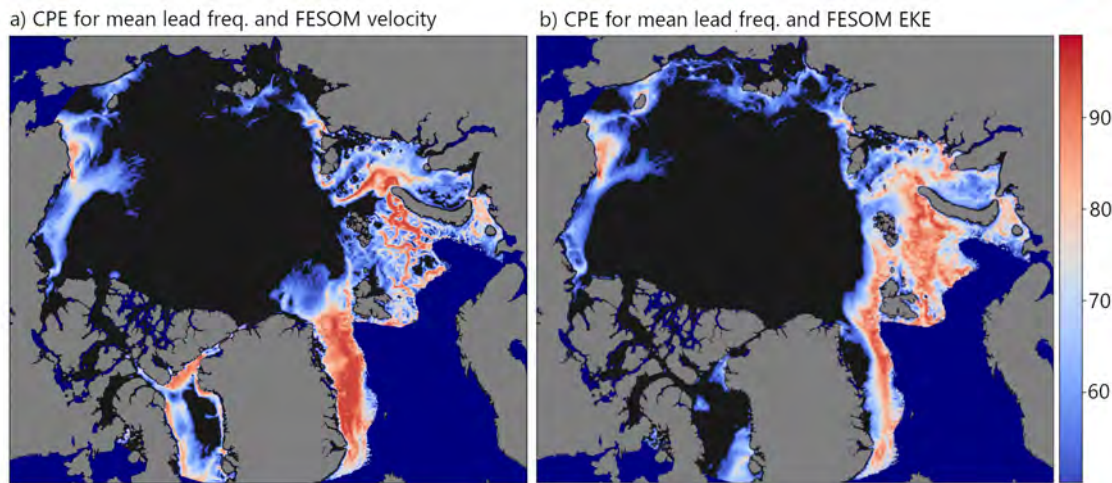
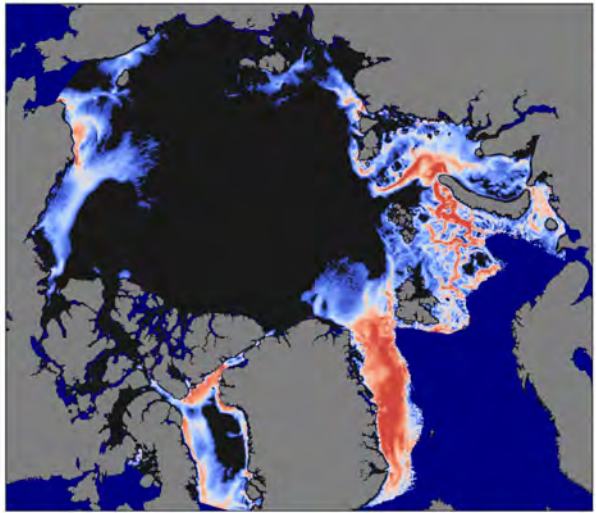


Figure 8. The Coincident Percentile Exceedance (CPE) for the mean wintertime lead frequency 2002-2016 and a) FESOM surface current velocity (F_SCV) and b) FESOM EKE (F_EKE). Values indicate the value percentile per pixel that exceeds in both data sets coincidentally and are cut off at values below the 50% percentile (black areas).

240 LFQ values. Many more interesting details can be seen in the two maps in Figure 8 that provide insight into how F_SCV and F_EKE affect the long-term lead dynamics individually and in which regions the stability of sea ice seems to be more prone to processes in the ocean.

a) CPE for mean lead freq. and FESOM velocity



b) CPE for mean lead freq. and FESOM EKE

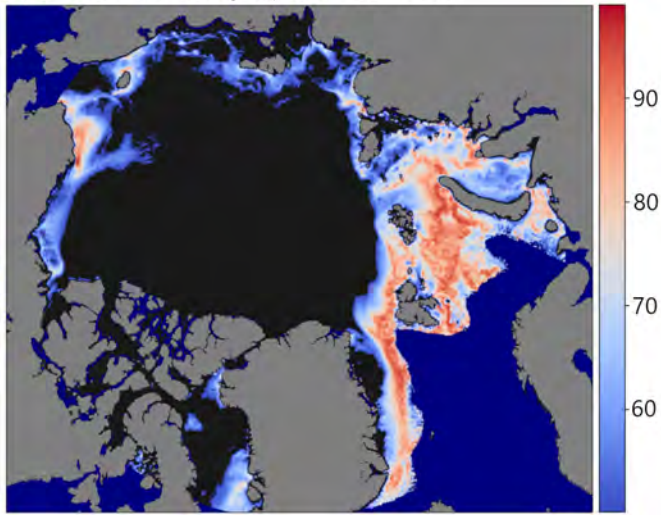
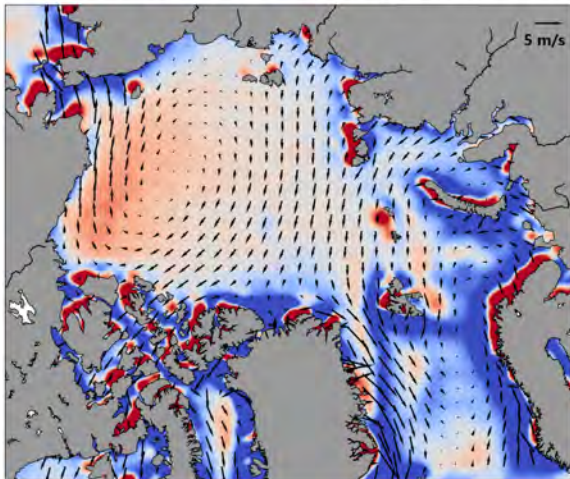


Figure 6. The Coincident Percentile Exceedance (CPE) for the mean wintertime lead frequency 2002-2016 and a) FESOM surface current velocity (F_SCV) and b) FESOM EKE (F_EKE). Values indicate the value percentile per pixel that exceeds in both data sets coincidentally.

a) ERA5: mean wind vectors and divergence, 2002-2021



b) C15: mean wind vectors and divergence, 2002-2016

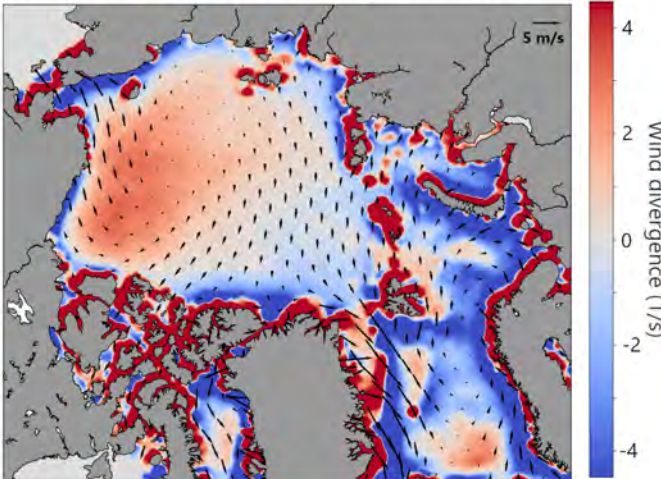


Figure 7. Spatial fields of mean wind divergence (in 10^{-6} s^{-1}) and mean horizontal wind vectors for a) ERA5, 2002-2021 (Hersbach et al., 2020) and b) C15, 2002-2016, for November to April. Wind vectors are shown with a spatial distance of 15 grid points for ERA5 and 10 grid points for C15, respectively (wind vector scale in the upper right corner)

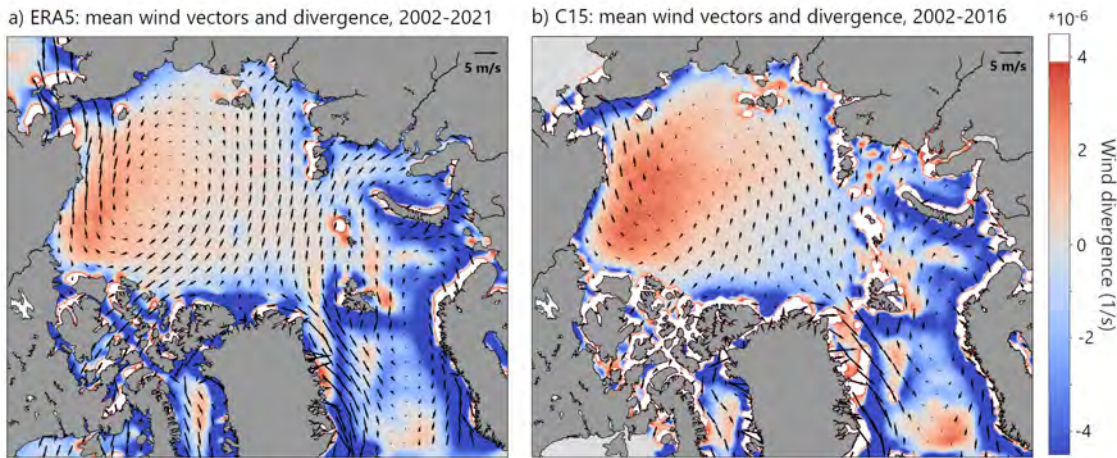


Figure 9. Spatial fields of mean wind divergence (in 10^{-6}s^{-1}) and mean horizontal wind vectors for a) ERA5, 2002-2021 (Hersbach et al., 2020) and b) C15, 2002-2016, for November to April. Wind vectors are shown with a spatial distance of 15 grid points for ERA5 and 10 grid points for C15, respectively (wind vector scale in the upper right corner). Regions with values exceeding $4 \times 10^{-6} \text{ 1/s}$ are masked out (white areas), since they are influenced by the transition of land to ocean in coastal areas and different resolutions of the associated land masks in most cases.

3.2.5 Spatial lead patterns and winds

The presented results indicate that the effect of the ocean on sea-ice lead dynamics is most obvious in the long-term, that is, in
 245 the climatology. This is argued for by comparing IBCAO ocean depth with the mean fields of LFQ, F_SCV and F_EKE. As far
 as the atmosphere is concerned, average wind speed and shear (not shown) provide no indication of driving the observed spatial
 patterns in the lead climatology on a pan-Arctic scale. However, the mean wind divergence (Figure 9) shows a dominant region
 of positive divergence centred around the Beaufort Gyre. This divergence pattern with maxima especially in the southern
 Beaufort Sea, is well aligned with the Beaufort Sea LFQ maximum indicated in Figure 1b. This broad region of generally
 250 increased lead occurrences might therefore be influenced by the mean divergence of the wind field rather than by ocean
 currents. Also, Fram Strait is characterized by a positive wind divergence in the long-term mean that can consequently add up
 to the influence of enhanced ocean currents on average lead frequencies in this region. In general, however, winds seem to have
 a larger effect on the temporal dynamics of leads rather than on the mean spatial patterns. This will be presented in detail in
 section 3.3.

255 3.2.6 Winds vs. ocean forcing in the mean lead fields

As shown above, the spatial patterns in the lead climatology show a strong coincidence with the spatial patterns of maxima
 in ocean surface currents and EKE. A link to mean winds can only be found in the fields of mean wind divergence and is
 constrained to the Beaufort Sea and Fram Strait. FESOM allows to distinguish between local forcing provided by winds and

3.2 Spatio-temporal lead variability

The MODIS lead climatology (Reiser et al., 2020) allows for an in-depth overview of wintertime sea-ice dynamics during the last two decades. As shown in Figure 8a, no overall trend is present in pan-Arctic monthly lead fractions (LFA). However, a significant seasonal and inter-annual variability can be noted with the tendency of a generally lower lead fraction at the end of winter (April) with frequency values of 0.1 on average compared to 0.15 in November. This is a reasonable finding considering the ice becoming thicker, more compact, and thus less mobile throughout the winter months. Subfigures 8b – 8i show the inter-annual and seasonal variability of lead fractions for individual regions (see map in Fig. 8a). None of the presented regions exhibits a significant trend. The magnitude of LFA differs between regions with the largest area covered by leads found in the FS sector (>0.5, note the different scales for individual regions). A strong seasonal variability is present in all regions, which is also indicated by the seasonal evolution of lead fractions per region (right panel for each region). While the change in area covered by leads is less pronounced in the FS, CN and BK sectors throughout winter, all other regions are characterized by a continuous decrease in lead fractions from November to April. In the central Arctic (CA) lead fractions are the lowest (<0.1 on average) and rather stable from November to March, but a significant drop is present from March to April, when lead fraction here is on average only around 0.05. Outliers in monthly lead fractions in all sectors indicate that strong anomalies are found only on the monthly scale, while there is no full year with extremely anomalous lead fractions on the pan-Arctic and on the regional scale.

This finding is presented in more detail in latitude-averaged monthly LFQ anomalies in 5° longitude bins for Nov 2002 to April 2021. Figure 9a shows the temporal evolution of LFQ anomalies in sea-ice regions between 70°N and 90°N across longitudes in the Arctic Ocean (the coastlines below the Figure indicate the respective position across longitudes). Also here, trends cannot be identified. The most interesting feature here is an indication of significant lead events that are expressed through strong positive anomalies (red dots). Several of these events can be identified from the diagram across all longitudes while the Siberian sector of the Arctic (90°E - 180°E) is generally characterized by a variability that is less pronounced than in other sectors. Two events are exemplarily extracted and shown as monthly lead anomaly maps. In Figure 9b, the monthly LFQ map shows strong anomalies north of the Canadian Archipelago with values of up to 15% above average (see marker b for comparison in Fig. 9a). An extreme lead event in the Beaufort Sea with similar anomalies is shown in Figure 9c (marker c in Fig. 9a), which resulted from a persistent high-pressure system over the central Arctic Ocean causing and intensification of the Beaufort Gyre (Babb et al., 2019). While the here presented short-term, i.e. monthly, variability of sea-ice leads is surely driven by many factors we here want to analyse the contribution of winds, i.e. wind speed and wind divergence.

3.3 Sea-ice leads and winds

To get a better insight into the driving mechanism for the temporal lead variability discussed above we investigate the grid-point correlation of monthly LFQ with wind from ERA5 and C15 model data, respectively. No significant correlations are found for the wind speed and wind shear (not shown). The Pearson correlation coefficient for monthly LFQ with wind divergence is shown in Figure 10 for ERA5 and C15, respectively. The latter is only available for the period 2002-2016. Only significant

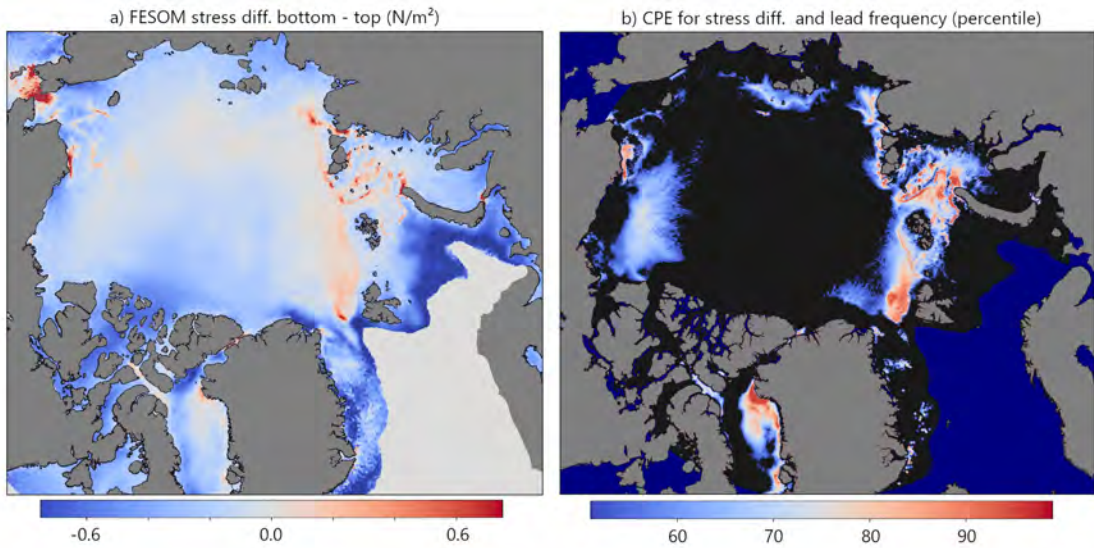


Figure 10. a) FESOM sea-ice stress difference bottom - top, b) Coincident Percentile Exceedance (CPE) of the FESOM stress difference and mean lead frequency.

ocean individually in terms of sea-ice surface and sea-ice bottom stress. The FESOM stress difference (bottom stress - top stress) is given in Figure 10a. Here, we can see that the modeled stress fields show the highest difference (with sea-ice bottom stress exceeding sea-ice surface stress) right where the observed lead frequencies are characterized by their most dominant patterns, i.e, the shelf break north of Franz-Josef Land, the eastern slop of St. Anna Trough, Vilitzky Strait and the western part of the Laptev Sea shelf break as well as Herald Canyon in the Chuckchi Sea. The regions where the stress difference is positive (ocean dominates) are coincident with high lead frequencies are highlighted in Figure 10b, which in comparison with

Figure 8, provides evidence for where the ocean plays a dominant role in shaping the mean lead patterns in the observed lead climatology. The region north and east of Point Barrow with its high mean lead frequencies is apparently characterized by a mixture of ocean and wind stress dominating here, while bathymetry and coastal geometry seem to act as two factors for lead opening/closing dynamics superimposed to one another. While the role of atmospheric forcing here was thoroughly analysed and presented recently, e.g. by Jewell et al. (2023), the influence of ocean process and batyhmetry requires additional research. Untangling individual regional forcings for lead dynamics will generally need an in-depth analysis that includes mechanistic explanations of dynamics, thermodynamics and the influence of coastal geometry.

3.3 Sea-ice leads and winds / temporal variability

To get a better insight into the driving mechanism for the temporal lead variability discussed above we investigate the grid-point correlation of monthly LFQ with wind from ERA5 and C15 model data, respectively. No significant correlations are found for the wind speed and wind shear (not shown). The Pearson correlation coefficient for monthly LFQ with wind divergence is

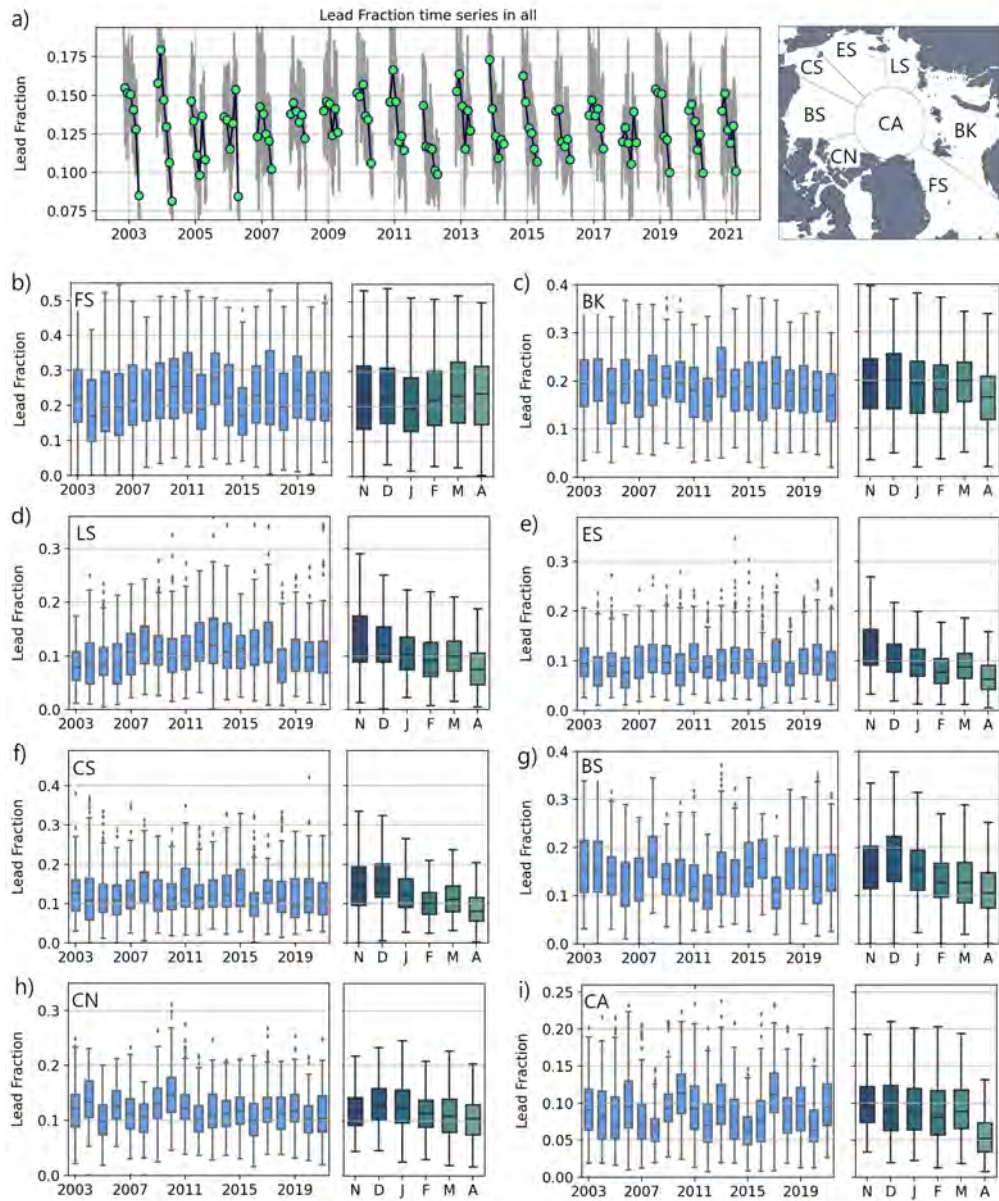


Figure 8. a) Time series of daily (grey) and monthly (green) Arctic lead fractions, all areas: Inset map indicates individual regions. b)-f) Lead fractions for individual regions throughout years and months for regions indicated in inset map: Fram Strait (FS), Barents and Kara Seas (BK), Laptev Sea (LS), East Siberian Sea (ES), Chuckchi Sea (CS), Beaufort Sea (BS), Canadian Arctic (CN), Central Arctic (CA). Left panels: box-whisker plots for individual years with median, the 25 and 75% percentiles as the box, the 10 and 90% percentiles are plotted as error bars. Right panels: as left panels, but for individual months.

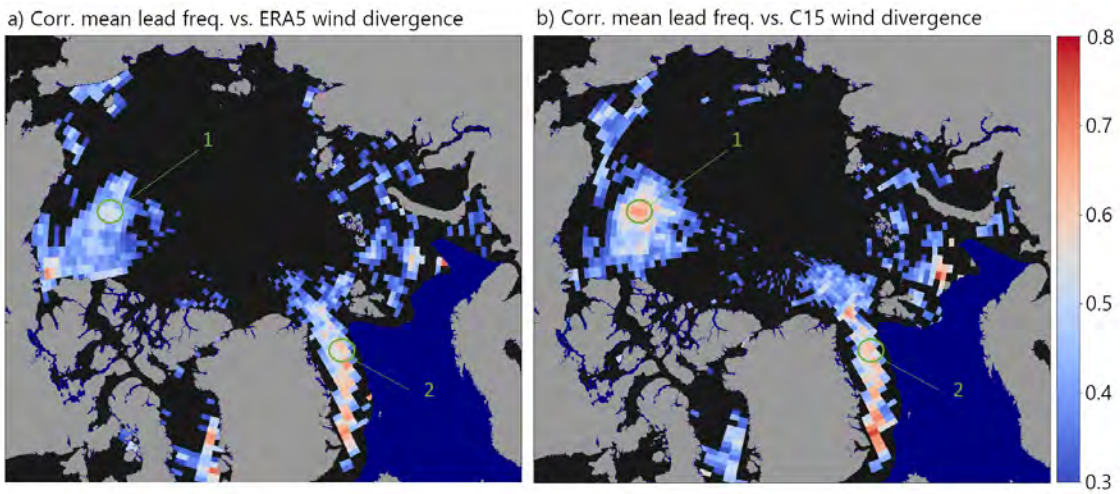


Figure 11. Pearson correlation for monthly values of mean lead frequency and monthly mean wind divergence from a) ERA5 (Hersbach et al., 2020), 2002-2020 (Nov-Apr) and b) C15, 2002-2016 (Nov-Apr). Coefficients are only shown for p-values<0.05.

shown in Figure 11 for ERA5 and C15, respectively. The latter is only available for the period 2002-2016. Only significant sectors are considered in both maps (p-values > 0.05). There are clearly two main regions, where a significant correlation between wind divergence and lead dynamics can be identified: Both, in the Beaufort Sea and in Fram Strait, the variability of monthly wind divergence correlates with the mean monthly lead frequency. While the correlation coefficient is generally only in the range between 0.5 and 0.7, the clustering of values in the two mentioned regions indicate that wind divergence is a significant driver of lead dynamics here. For the C15 data, there is a maximum correlation in the approximate center of the Beaufort Gyre (Fig. 11b), while this is less pronounced with ERA5 data (Fig. 11a). Towards Fram Strait, correlations increase southward.

No significant correlation is found in the central and Siberian Arctic, suggesting that on average winds play only a minor role in the regional lead dynamics for these sectors. The Barents and Kara Seas indicate some sectors with significant correlation with a maximum at the ice edge. Two points are indicated (1: central Beaufort Sea, 2: Fram Strait) from where time series are extracted to show the temporal evolution of monthly values of LFQ and wind divergence from ERA5 and C15, respectively. Figure 12 shows the evolution of monthly averages of these data at points 1 and 2 in Figure 11 for November to April, 2002-2021 (ERA5) and 2002-2016 (C15). The comparison of time series suggests that peaks in the mean LFQ (grey) are very often accompanied by high average wind divergence (blue and orange). This is also confirmed by the associated scatterplots on the right-hand side of the time series panels, where a positive correlation between wind divergence and LFQ is indicated for both ERA5 and C15 data, respectively. In Point 1 (Beaufort Sea), the correlation coefficient is 0.67 for LFQ with C15 data and 0.54 for LFQ with ERA5 data. In Point 2 (Fram Strait) these values are 0.69 and 0.61, respectively (Note that p-values for all coloured points in Figure 12 are < 0.05). Figure 9 puts this in context with the fields of mean divergence and mean horizontal wind vectors from ERA5 and C15 data sets. If the coastal regions are not considered (where the effects due to friction and

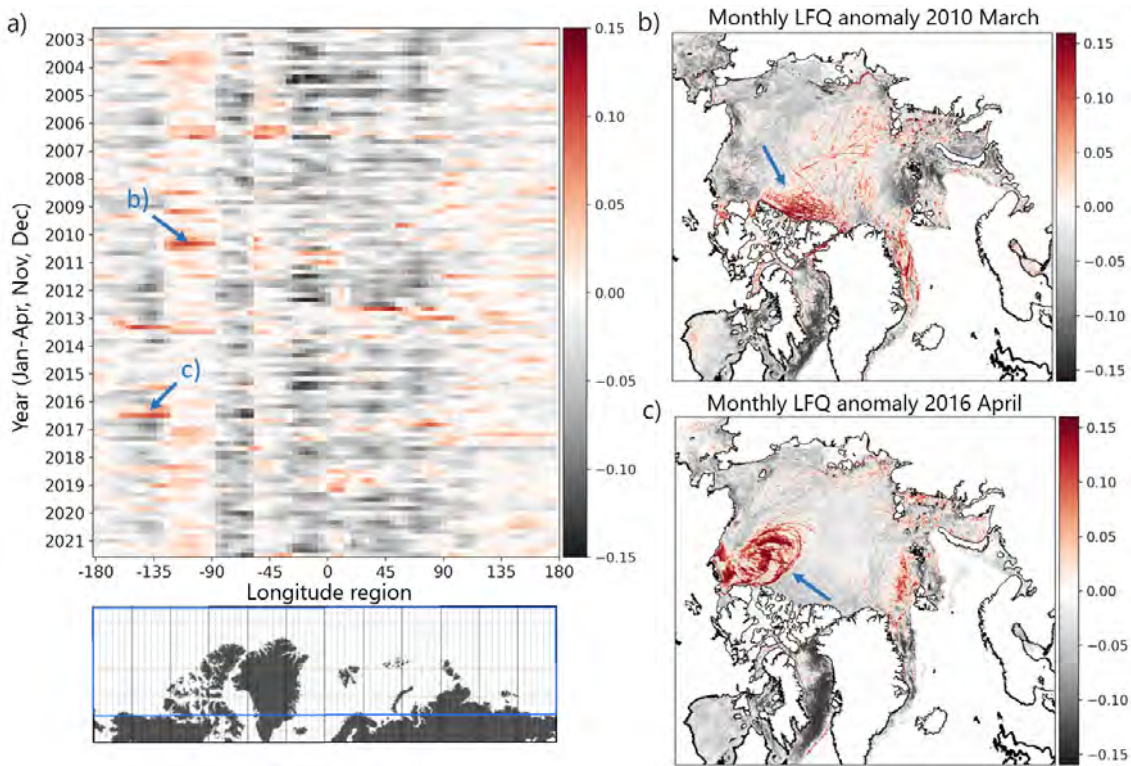


Figure 9. a) Latitude-averaged (70-90°N) monthly LFQ anomalies in 5° longitude bins for Nov 2002 to April 2021. Only the months Nov, Dec, Jan, Feb, Mar and Apr are shown, b) monthly lead frequency (LFQ) anomaly for 2010, Mar, with a very strong positive lead anomaly north of the Canadian Archipelago and c) monthly LFQ anomaly for 2016, April, underpinning the strong positive lead anomaly in the Beaufort Sea that is also given in the overview in a).

240 sectors are considered in both maps (p -values > 0.05). There are clearly two main regions, where a significant correlation
 between wind divergence and lead dynamics can be identified: Both, in the Beaufort Sea and in Fram Strait, the variability
 of monthly wind divergence correlates with the mean monthly lead frequency. While the correlation coefficient is generally
 only in the range between 0.5 and 0.7, the clustering of values in the two mentioned regions indicate that wind divergence
 is a significant driver of lead dynamics here. For the C15 data, there is a maximum correlation in the approximate center of
 245 the Beaufort Gyre (Fig. 10b), while this is less pronounced with ERA5 data (Fig. 10a). Towards Fram Strait, correlations are
 increasing towards South.

No significant correlation is found in the central and Siberian Arctic, suggesting that on average winds play only a minor role
 in the regional lead dynamics for these sectors. The Barents and Kara Seas indicate some sectors with significant correlation
 with a maximum at the ice edge. Two points are indicated (1: central Beaufort Sea, 2: Fram Strait) from where time series are
 250 extracted to show the temporal evolution of monthly values of LFQ and wind divergence from ERA5 and C15, respectively.
 Figure 11 shows the evolution of monthly averages of these data at points 1 and 2 in Figure 10 for November to April, 2002-

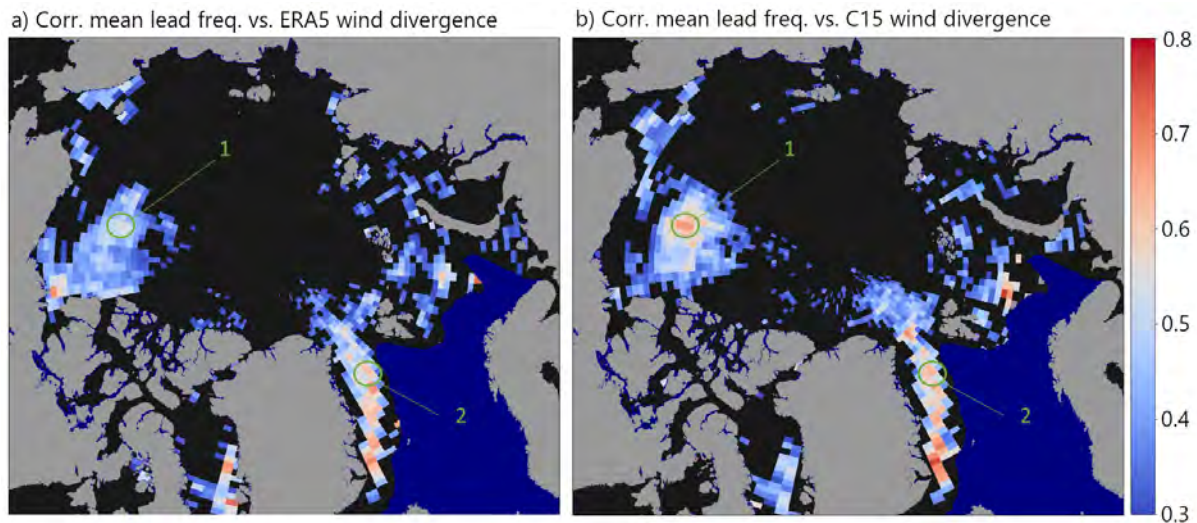


Figure 10. Pearson correlation for monthly values of mean lead frequency and monthly mean wind divergence from a) ERA5 (Hersbach et al., 2020), 2002-2020 (Nov-Apr) and b) C15, 2002-2016 (Nov-Apr). Coefficients are only shown for p -values < 0.05 .

2021 (ERA5) and 2002-2016 (C15). The comparison of time series suggests that peaks in the mean LFQ (grey) are very often accompanied by high average wind divergence (blue and orange). This is also confirmed by the associated scatterplots on the right-hand side of the time series panels, where a positive correlation between wind divergence and LFQ is indicated for both ERA5 and C15 data, respectively. In Point 1 (Beaufort Sea), the correlation coefficient is 0.67 for LFQ with C15 data and 0.54 for LFQ with ERA5 data. In Point 2 (Fram Strait) these values are 0.69 and 0.61, respectively. Figure 7 puts this in context with the fields of mean divergence and mean horizontal wind vectors from ERA5 and C15 data sets. If the coastal regions are not considered (where the effects due to friction and topography dominate), the main maximum in mean wind divergence is found in the Beaufort Sea. This maximum is associated with the mean anticyclonic circulation of the Beaufort high and is more pronounced in the C15 data. The mean wind vector fields reflect also the Transpolar Drift from the Laptev Sea to Fram Strait and the southward winds with high directional constancy over Fram Strait.

4 Discussion

With the perspective of a changing Arctic, knowledge about the drivers of wintertime sea-ice dynamics is key. In this context, insight about where and when leads are forming and an overview about the conditions that favour the formation of leads are essential. When extreme sea-ice break-up events are observed, the focus is most often set on explaining the driving mechanisms (Rheinlaender et al., 2022; Babb et al., 2019), which are generally strong winds and/or waves. Also in some studies, the attribution of overall anthropogenic influences on extreme events in Arctic sea ice is analyzed (Kirchmeier-Young et al., 2017). In any case, the drivers for sea-ice dynamics on seasonal and inter-annual time scales are found in ocean processes and in the

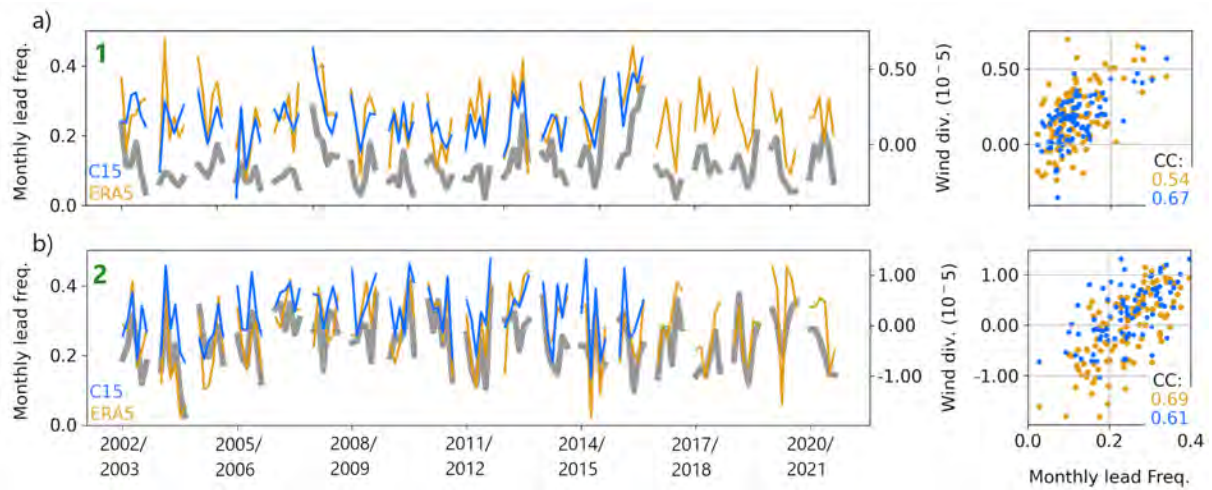


Figure 12. Time series of monthly and sectoral averages of lead frequency (grey) and wind divergence from ERA5 (Hersbach et al., 2020; orange) and C15 (blue) as well as associated scatterplots for a) Point 1 and b) Point 2 in Figure 11. Correlation coefficients are indicated in the scatterplots for LFQ with ERA5 (orange) and C15 (blue).

topography dominate), the main maximum in mean wind divergence is found in the Beaufort Sea. This maximum is associated with the mean anticyclonic circulation of the Beaufort high and is more pronounced in the C15 data. The mean wind vector fields reflect also the Transpolar Drift from the Laptev Sea to Fram Strait and the southward winds with high directional constancy over Fram Strait.

300 4 Discussion

With the perspective of a changing Arctic, knowledge about the drivers of wintertime sea-ice dynamics is key. In this context, insight about where and when leads are forming and an overview about the conditions that favour the formation of leads are essential. When extreme sea-ice break-up events are observed, the focus is most often set on explaining the driving mechanisms (Rheinlaender et al., 2022; Babb et al., 2019), which are generally strong winds or (in the marginal ice zone) waves (e.g., 305 Pavlova et al., 2014). Also in some studies, the attribution of overall anthropogenic influences on extreme events in Arctic sea ice is analyzed (Kirchmeier-Young et al., 2017). In any case, the drivers for sea-ice dynamics on seasonal and inter-annual time scales are found in ocean processes and in the atmosphere. However, the relative importance of oceanic and atmospheric processes for changes in the Arctic sea-ice cover is not well established (Liu et al., 2022). In this study, we therefore present a 310 first attempt to describe and untangle the influence of both drivers spatially and temporally. The drift of sea ice and the associated stress is directly connected to the formation of leads. The main circulation patterns of Arctic sea ice, the Beaufort Gyre and the Transpolar Drift, have shown a net strengthening during last decades, which was attributed mainly to a reduced multiyear sea-ice cover (Kwok et al., 2013, Stroeve and Notz, 2018). Younger and thinner ice is expected to be more prone to break-up and

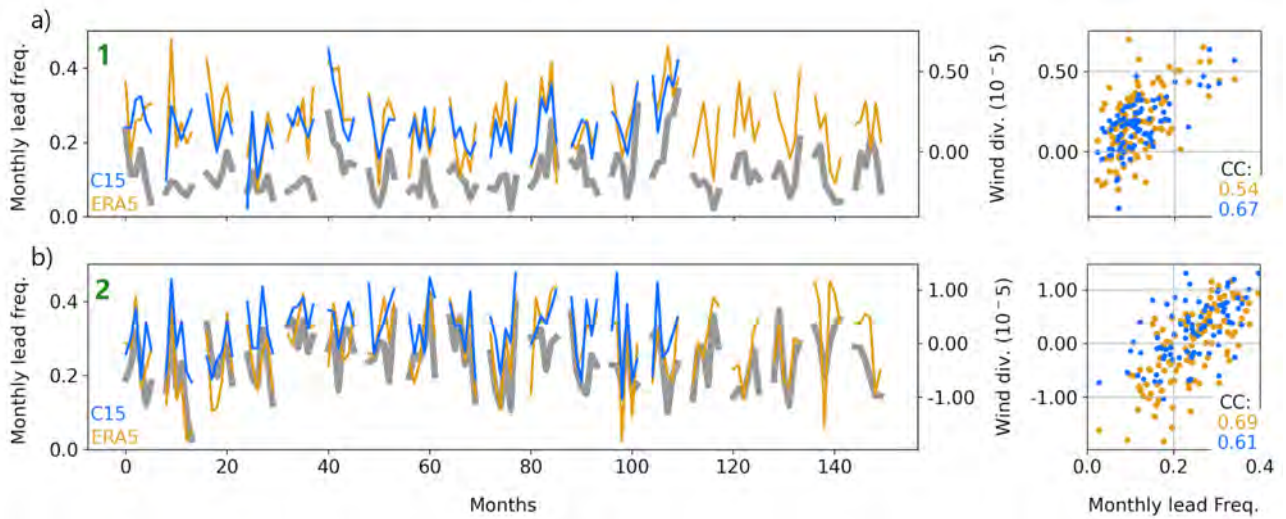


Figure 11. Time series of monthly and sectoral averages of lead frequency (grey) and wind divergence from ERA5 (Hersbach et al., 2020; orange) and C15 (blue) as well as associated scatterplots for a) Point 1 and b) Point 2 in Figure 10. Correlation coefficients are indicated in the scatterplots for LFQ with ERA5 (orange) and C15 (blue).

atmosphere. However, the relative importance of oceanic and atmospheric processes for changes in the Arctic sea-ice cover is

270 not well established (Liu et al., 2022). In this study, we therefore present a first attempt to describe and untangle the influence of both drivers spatially and temporally. The drift of sea ice and the associated stress is directly connected to the formation of leads.

The main circulation patterns of Arctic sea ice, the Beaufort Gyre and the Transpolar Drift, have shown a net strengthening during last decades, which was attributed mainly to a reduced multiyear sea-ice cover (Kwok et al., 2013, Stroeve and Notz, 2018). Younger and thinner ice is expected to be more prone to break-up and lead formation (Zhang et al., 2012). However,

275 we could not observe trends in monthly wintertime lead fractions in the period between 2002 and 2021 (see Figure 8). A small positive lead area trend of 3700 km^2 per year was reported by Hoffmann et al. (2022), however with a large uncertainty and based on a different lead climatology, which shows less of the patterns highlighted in this study. Eicken et al. (2012) describe

an increase in lead frequency in the Beaufort Sea in the period of 2004–2010 in comparison to 1993–2004. They explain this finding with less multi-year ice and increased divergence (Hutchings and Rigor, 2012; Babb et al., 2022). From the data we

280 present here, an increase of lead frequencies in the Beaufort Sea cannot be inferred, but as our analysis does not include lead observations before 2002, no conclusion can be drawn about changes in comparison to the period prior to this year.

4.1 Winds and leads

The role of storms and waves on wintertime sea-ice break up is well known. We could, however, not find an overall correlation between leads and wind speed in long-term data although their relation is well documented for several case studies, at least

285 for shorter time scales and extreme events (e.g., Graham et al., 2019, Rheinlaender et al., 2022). Instead, we find the wind

lead formation (Zhang et al., 2012). However, we could not observe trends in wintertime lead fractions in the period between 2002 and 2021 (see Figure 2). A small positive lead area trend of 3700 km^2 per year was reported by Hoffmann et al. (2022), 315 however with a large uncertainty and based on a different lead climatology, which shows less of the patterns highlighted in this study. Eicken et al. (2012) describe an increase in lead frequency in the Beaufort Sea in the period of 2004–2010 in comparison to 1993–2004. They explain this finding with less multi-year ice and increased divergence (Hutchings and Rigor, 2012; Babb et al., 2022). From the data we present here, an increase of lead frequencies in the Beaufort Sea cannot be inferred, but as 320 our analysis does not include lead observations before 2002, no conclusion can be drawn about changes in comparison to the period prior to this year. In Lewis and Hutchings (2019), no trend in occurrence of leads in the Beaufort Sea is found over 20 winters from December 1993 to May 2013. The trends in leads we find in this analysis are constrained to individual months and regions and are partly even negative (see Section 3.1).

4.1 Winds and leads

The role of storms and waves on wintertime sea-ice break up is well known (e.g., Graham et al., 2019). We could, however, 325 not find an overall correlation between leads and wind speed in long-term data although their relation is well documented for several case studies, at least for shorter time scales and extreme events (e.g., Rheinlaender et al., 2022). Instead, we find the wind divergence to be a dominant driver for large-scale lead dynamics and sea-ice variability. We therefore assume the influence of wind speed on large-scale lead formation to be confined to short time scales and divergent conditions, at least for cases when the ice cover is still dense and compact. On the other hand, increasing wind speeds are projected for the future 330 wintertime Arctic in conditions with a less dense sea ice cover and consequent surface warming (Mioduszewski et al., 2018). Thus, a potentially enhanced sea-ice loss and increasing lead fractions can be amplified by the resulting intensified winds in the future. In the Barents and Kara Seas with their marginal ice zones we find generally high lead frequencies. Here, the influence of winds affects the redistribution of sea ice and thereby the formation of leads (Pavlova et al., 2014). From the ocean side, the advection of heat through winds can trigger a thermodynamic weakening of the sea-ice cover, which can favour a 335 break-up in regions of strong surface gradients. We find high lead frequencies also in Fram Strait, where ice export is directly connected to higher southward ice drift velocities, due to stronger geostrophic winds (Smedsrød et al., 2011). Our findings show that also here, the enhanced lead activity can be attributed to strong ocean surface currents (in the climatology) and to wind divergence on seasonal scales (Figures 6 and 10). In the Beaufort Sea, we find a large region of enhanced lead activity around the Beaufort Gyre, that shows significant correlation with wind divergence. High sea-ice divergence in this region is 340 reported also by Wang et al. (2016) based on FESOM simulations with 4.5 km horizontal resolution in the Arctic and by Spreen et al. (2017) based on RADARSAT satellite data. The finding that changes in sea ice coverage in the Beaufort Sea are primarily wind driven was also reported by Frey et al. (2015). While the correlation of changes in sectoral monthly LFQ anomalies with monthly wind data shows significance only for wind divergence in the given regions in this analysis (Figure 11), we have to make clear that an in-depth analysis of winds and leads will potentially offer a more detailed insight. In this 345 context, the lower spatial resolution of the atmospheric data (15 km and 30 km, for C15 and ERA5, respectively) in comparison to FESOM (up to 4.5 km) needs to be mentioned as a potential factor for blurring fine-scale variabilities. In individual regions

divergence to be a dominant driver for large-scale lead dynamics and sea-ice variability. We therefore assume the influence of wind speed on large-scale lead formation to be confined to short time scales and divergent conditions, at least for cases when the ice cover is still dense and compact. On the other hand, increasing wind speeds are projected for the future wintertime Arctic in conditions with a less dense sea ice cover and consequent surface warming (Mioduszewski et al., 2018). Thus, a potentially enhanced sea-ice loss and increasing lead fractions can be amplified by the resulting intensified winds in future. In the Barents and Kara Seas with their marginal ice zones we find high lead frequencies all over. Here, the influence of winds affects both the redistribution of sea ice and the formation of leads (Pavlova et al., 2014). From the ocean side, the advection of heat through winds can trigger a thermodynamic weakening of the sea-ice cover, which can favour a break-up in regions of strong surface gradients (compare Figure 6). We find high lead frequencies also in Fram Strait, where ice export is directly connected to higher southward ice drift velocities, due to stronger geostrophic winds (Smedsrød et al., 2011). Our findings show that also here, the enhanced lead activity can be attributed to strong ocean surface currents (in the climatology) and to wind divergence on seasonal scales (Figures 6 and 10). In the Beaufort Sea, we find a large region of enhanced lead activity around the Beaufort Gyre, that shows significant correlation with wind divergence. High sea-ice divergence in this region is reported also by Spreen et al. (2017) based on RADARSAT satellite data. The finding that shifts in sea ice cover in the Beaufort Sea are primarily wind driven was also reported by Frey et al. (2015). Qu et al. (2021) discuss a positive interannual trend in the April lead area of the Beaufort Sea and close relation to enhanced ice motion driven by an enhanced Beaufort High and persistent easterly winds. This reported monthly trend cannot be seen in our annual time series (Figure 8g).

4.2 Ocean and leads

The spatial patterns in mean lead frequencies (Figure 2a) seem to be significantly affected by ocean bathymetry and the Arctic Circumpolar Boundary Current (Aksенов et al., 2011; Pnyushkov et al., 2015), especially with its Barents Sea branch and its pathways along the shelf break. While we can assume that it's not the heat of the Atlantic water directly that triggers increased sea-ice break up, it might well be intensified currents and tide-induced shear (Janout et al., 2015; Årthun et al., 2019). Tides are not included in the FESOM simulations, which means that the contribution of this component could even enhance the suggested governing role of the ocean on preconditioning the sea-ice stability. Holloway and Proshutinsky (2007) show that tides are capable of enhancing the loss of heat from Atlantic waters. The impact of tides on sea ice is characterized by an enhanced ocean heat flux that causes a general sea-ice thinning and thereby makes the ice more prone to lead formation. This suggests that a lot of the lead patterns that can be seen in Figure 2a are due to so-called tidal leads. The fine details in the spatial lead patterns that can be seen in our lead climatology (see Figures 3, 4, 5) have probably the potential to reveal much more of what is happening in the ocean and about the pathways and branches of water masses that could hitherto only be described with model and mooring data. For the eastern Arctic Ocean, i.e. the Laptev Sea and northern Kara Sea, an increased oceanic heat flux from intermediate-depth warm Atlantic Water to the surface mixed layer and sea ice was reported by Polyakov et al. (2020). Such a warming at the ocean surface has the potential for a thermodynamic weakening of sea ice in these regions, which can add up to the already present dynamic weakening through changing water masses and strong surface gradients. Consequently, while trends cannot be observed in the eastern Arctic Ocean in the present study, lead fractions are likely to

and for certain periods and events, strong wind speeds and thin ice (Jewell and Hutchings, 2023) as well as the location and trajectory of pressure systems (e.g., Aue et al., 2022) and the effect of coastal geometry (Lewis and Hutchings, 2019) will definitely play a significant role in the opening and closing of leads. Only recently, Jewell et al. (2023) have demonstrated, how 350 coastal boundaries modify the response of sea-ice dynamics to wind forcing. Generally speaking, it will require an in-depth analysis that includes mechanistic explanations of dynamics, thermodynamics and the influence of coastal geometry to be able to identify individual regional forcings for lead dynamics.

4.2 Ocean and leads

The spatial patterns in mean lead frequencies (Figure 1b) seem to be significantly affected by ocean bathymetry and the Arctic 355 Circumpolar Boundary Current (Aksenov et al., 2011; Pnyushkov et al., 2015), especially with its Barents Sea branch and its pathways along the shelf break. While we can assume that it's not the heat of the Atlantic water directly that triggers increased sea-ice break up, it might well be intensified currents and tide-induced shear (Janout et al., 2015; Årthun et al., 2019). Tides are not included in the FESOM simulations, which means that the contribution of this component could even enhance the 360 suggested governing role of the ocean on preconditioning the sea-ice stability. Holloway and Proshutinsky (2007) show that tides are capable of enhancing the loss of heat from Atlantic waters. The impact of tides on sea ice is characterized by an enhanced ocean heat flux that causes a general sea-ice thinning and thereby makes the ice more prone to lead formation. This suggests the hypothesis that some of the lead patterns that can be seen in Figure 1b are due to so-called tidal leads. This can, 365 however, not be answered with the presented analysis. The fine details in the spatial lead patterns that can be seen in our lead climatology (see Figures 5, 6, 7) have probably the potential to reveal much more of what is happening in the ocean and about the pathways and branches of water masses that could hitherto only be described with model and mooring data.

For the eastern Arctic Ocean, i.e. the Laptev Sea and northern Kara Sea, an increased oceanic heat flux from intermediate-depth warm Atlantic Water to the surface mixed layer and sea ice was reported by Polyakov et al. (2020). Such a warming at the ocean surface has the potential for a thermodynamic weakening of sea ice in these regions, which can add up to the already present dynamic weakening through changing water masses and strong surface gradients. Consequently, while positive trends 370 can be observed in the eastern Arctic Ocean in the present study only in November, lead fractions are likely to increase here when increased oceanic heat fluxes persist. In the Chuckchi Sea, the ocean currents and branches described by e.g. Stabeno et al., (2018) clearly resemble the observed spatial lead patterns. Herald canyon, Barrow canyon as well as Herald and Hanna Shoals are the main bathymetric features in this region that govern the ocean currents. We argue here that surface gradients and eddy kinetic energies in these regions are responsible for a frequent formation of sea-ice leads at or next to these structures. 375 The interaction between ocean and leads occurs in two ways. As shown here, the ocean acts as a preconditioner for sea ice break-up, the resulting leads will in turn affect ocean stratification through new ice formation and eddy formation with an associated horizontal redistribution of salinity anomalies (Cohanim et al., 2021). Recently, interactions between ocean-ice heat fluxes, sea ice cover, and upper-ocean eddies were discussed and highlighted as a missing feedback in current climate models (Manucharyan and Thompson, 2022).

320 increase here when increased oceanic heat fluxes persist. In the Chuckchi Sea, the ocean currents and branches described by e.g. Stabeno et al., (2018) clearly resemble the observed spatial lead patterns. Herald canyon, Barrow canyon as well as Herald and Hanna Shoals are the main bathymetric features in this region that govern the ocean currents. We argue here that surface gradients and eddy kinetic energies in these regions are responsible for a frequent formation of sea-ice leads at or next to these structures. The interaction between ocean and leads occurs in two ways. As shown here, the ocean acts as a preconditioner for
325 sea ice break-up, the resulting leads will in turn affect ocean stratification through new ice formation and eddy formation with an associated horizontal redistribution of salinity anomalies (Cohanim et al., 2021). Recently, interactions between ocean-ice heat fluxes, sea ice cover, and upper-ocean eddies were discussed and highlighted as a missing feedback in current climate models (Manucharyan and Thompson, 2022).

4.3 Overall lead patterns and seasonal impacts

330 The presented lead climatology shows a lot of very interesting regional details that could not all be described and analysed in this paper. Especially over the shelf of the Barents and Kara Seas as well as in the East Siberian and Chuckchi Seas, very distinct but small-scale spatial patterns of mean lead frequencies indicate a significant preconditioning of the ice cover through the ocean and a strong role of bathymetry. These features deserve a thorough in-depth analysis to get a more detailed insight into how the ocean shapes the sea ice and into how projected anomalies of ocean processes in the future could affect the
335 sea-ice cover. It is also suggested that summer sea ice might be affected by deformation events of winter sea ice and the resulting fracturing (Korosov et al., 2022; Hwang et al., 2017). Zhang et al., 2018 show that a realistic representation of sea ice leads in prediction systems has the potential for predicting the summer Arctic sea ice extent. With the presented results we argue that seasonal lead dynamics are mainly driven by winds (e.g. Liu et al., 2022) with the wind divergence yielding the most significant correlations with temporal lead dynamics. The ocean, however, is highly responsible for preconditioning
340 the ice cover and making it more prone in some regions for thinning and break-up than in others with a distinct influence of bathymetry.

5 Conclusions

We here present the first analysis of the drivers for the spatial and temporal patterns of Arctic sea-ice leads based on a 20-years climatology from satellite observations with a 1 km^2 spatial resolution. No long-term trends can be identified for regional
345 or pan-Arctic average wintertime sea-ice lead fractions in the period from 2002 to 2021. In most regions, the monthly lead fractions decrease on average slightly towards the end of winter. The results of our analysis reveal a strong influence of ocean depth and associated currents on the frequency of occurrence of leads. This suggests that the ocean acts a preconditioner for sea-ice break-up through dynamic processes mainly over the shelf break, along channels and slopes and over shoals. Moreover, we find indication that regions with a high average wind field divergence, i.e. the Beaufort Sea and Fram Strait are more
350 prone to lead formation than other regions. These regions are also characterized by a significant temporal correlation of the monthly wind field divergence and monthly lead frequencies, while wind speed and wind shear do not correlate with changes

The presented lead climatology shows a lot of very interesting regional details that could not all be described and analysed in this paper. Especially over the shelf of the Barents and Kara Seas as well as in the East Siberian and Chuckchi Seas, very distinct but small-scale spatial patterns of mean lead frequencies indicate a significant preconditioning of the ice cover through the ocean and a strong role of bathymetry. These features deserve a thorough in-depth analysis to get a more detailed insight 385 into how the ocean shapes the sea ice and into how projected anomalies of ocean processes in the future could affect the sea-ice cover. It is also suggested that summer sea ice might be affected by deformation events of winter sea ice and the resulting fracturing (Korosov et al., 2022; Hwang et al., 2017). With the presented results we argue that seasonal lead dynamics are mainly driven by winds (e.g. Liu et al., 2022) with the wind divergence yielding the most significant correlations with temporal 390 lead dynamics. The ocean, however, is highly responsible for preconditioning the ice cover and making it more prone in some regions for thinning and break-up than in others with a distinct influence of bathymetry. There are, however, many open 395 questions resulting from the presented analysis and comparison of model data and observed leads. For example: Why do strong ocean currents and bathymetry in some regions align with high lead frequencies and not in others, where and how does coastal geometry impact the opening and closing of the ice pack, which role does the trajectory of synoptic-scale pressure systems and associated wind fields play for lead dynamics on the short time scale and how will an anticipated thinning of Arctic sea ice change these interactions?

5 Conclusions

We here present a first interpretation of the drivers for the spatial and temporal patterns of Arctic sea-ice leads based on a 20-years climatology from satellite observations with a 1 km^2 spatial resolution. No long-term trends can be identified for 400 pan-Arctic average wintertime sea-ice lead fractions in the period from 2002 to 2021. On the regional scale and for individual months, however, both positive (LS/November, CA/November, ES/November, BS/April) and negative trends (BK/March, BS/February, CN/January, CN/February) can be found. In most regions, the monthly lead fractions decrease on average slightly towards the end of winter. The results of our analysis reveal a strong influence of ocean depth and associated currents on the frequency of occurrence of leads. This suggests that the ocean acts a preconditioner for sea-ice break-up through dynamic 405 processes mainly over the shelf break, along channels and slopes and over shoals. Moreover, we find indication that regions with a high average wind field divergence, i.e. the Beaufort Sea and Fram Strait are more prone to lead formation than other regions. These regions are also characterized by a significant temporal correlation of the monthly wind field divergence and monthly lead frequencies, while wind speed and wind shear do not correlate with changes in lead dynamics on long-term monthly time scales. We conclude from the presented results that the ocean (in conjunction with significant bathymetric features and associated currents) as well as a high mean wind divergence can prime the sea-ice in making it more vulnerable to 410 break-up. Thereby, leads are more likely to occur in these regions when synoptic conditions are appropriate. While we assume events with high wind speed to contribute strongly to lead formation, we find the wind divergence to represent these conditions better on the monthly time scale. For more detailed conclusions and to be able to identify individual regional forcings for lead

in lead dynamics on long-term monthly time scales. We can conclude from the presented results that the ocean (in conjunction with significant bathymetric features and associated currents) as well as a high mean wind divergence can prime the sea-ice in making it more vulnerable to break-up. Thereby, leads are more likely to occur in these regions when synoptic conditions 355 are appropriate. While we assume events with high wind speed to contribute strongly to lead formation, we find the wind divergence to represent these conditions better on the monthly time scale. The presented spatial patterns of the used Arctic lead climatology exhibit a lot of details that can be used for a more thorough regional analysis of air - sea ice – ocean interactions.

Data availability. The daily wintertime lead data for the period November 2002 to April 2021 are currently under consideration for publication as annual files in NetCDF format on PANGAEA (*ArcLeads: Daily sea-ice lead maps for the Arctic, 2002-2021, NOV-APR, DOI is 360 pending and will be included in the final version*). CCLM data are available in the World Data Centre for Climate (https://www.wdc-climate.de/ui/entry?acronym=DKRZ_LTA_474_dsg0001). Version 4.0 of the International Bathymetric Chart of the Arctic Ocean (IBCAO, Jakobs-son et al., 2020) was acquired from <https://gebco.net> and ERA5 data (Hersbach et al., 2020) were downloaded from the Copernicus Climate Data Store (<https://cds.climate.copernicus.eu/>).

Author contributions. SW analysed the data and drafted the main script. FS performed the FESOM simulations and EKE calculations. The 365 final version was prepared with contributions from all co-authors.

Competing interests. The authors declare that they have no conflict of interest.

Acknowledgements. The research was funded by the Deutsche Forschungsgemeinschaft (DFG) in the framework of the priority program “Antarctic Research with comparative investigations in Arctic ice areas” under grant WI 3314/3 and by the Federal Ministry of Education and Research (BMBF) under grant 03F0831C in the frame of German-Russian cooperation “WTZ RUS: Changing Arctic Transpolar System 370 (CATS)”. We acknowledge the CLM Community and the German Meteorological Service for providing the basic COSMO-CLM model. This work used resources of the Deutsches Klimarechenzentrum (DKRZ) granted by its Scientific Steering Committee (WLA) under project ID bb0474. The FESOM simulations were performed with resources provided by the North-German Supercomputing Alliance (HLRN). We thank Lukas Schefczyk for performing the CCLM simulations. The publication was funded / supported by the Open Access Fund of Universität Trier and by the German Research Foundation (DFG).

dynamics, it will be necessary to conduct in-depth analyses including mechanistic explanations of dynamics, thermodynamics and the influence of coastal geometry. The presented spatial patterns of the used Arctic lead climatology exhibit a lot of details
415 that can be used for a more thorough regional analysis of air - sea ice – ocean interactions.

Data availability. The daily wintertime lead data for the period November 2002 to April 2021 are currently under consideration for publication as annual files in NetCDF format on PANGAEA (*ArcLeads: Daily sea-ice lead maps for the Arctic, 2002-2021, NOV-APR*, <https://doi.pangaea.de/10.1594/PANGAEA.955561>). CCLM data are available in the World Data Centre for Climate (https://www.wdc-climate.de/ui/entry?acronym=DKRZ_LTA_474_dsg0001). Version 4.0 of the International Bathymetric Chart of the Arctic Ocean (IBCAO, Jakobsson
420 et al., 2020) was acquired from <https://gebco.net> and ERA5 data (Hersbach et al., 2020) were downloaded from the Copernicus Climate Data Store (<https://cds.climate.copernicus.eu/>).

Author contributions. SW analysed the data and drafted the main script. FS performed the FESOM simulations and EKE calculations. The final version was prepared with contributions from all co-authors.

Competing interests. The authors declare that they have no conflict of interest.

425 Acknowledgements. The research was funded by the Deutsche Forschungsgemeinschaft (DFG) in the framework of the priority program “Antarctic Research with comparative investigations in Arctic ice areas” under grant WI 3314/3 and by the Federal Ministry of Education and Research (BMBF) under grant 03F0831C in the frame of German-Russian cooperation “WTZ RUS: Changing Arctic Transpolar System (CATS)”. We acknowledge the CLM Community and the German Meteorological Service for providing the basic COSMO-CLM model. This work used resources of the Deutsches Klimarechenzentrum (DKRZ) granted by its Scientific Steering Committee (WLA) under project
430 ID bb0474. The FESOM simulations were performed with resources provided by the North-German Supercomputing Alliance (HLRN). We thank Lukas Schefczyk for performing the CCLM simulations. The publication was funded / supported by the Open Access Fund of Universität Trier and by the German Research Foundation (DFG).

Aksenov, Y., Ivanov, V. V., Nurser, A. J. G., Bacon, S., Polyakov, I. V., Coward, A. C., Naveira-Garabato, A. C., and Beszczynska-Moeller, A.: The Arctic Circumpolar Boundary Current, *Journal of Geophysical Research: Oceans*, 116, <https://doi.org/10.1029/2010JC006637>, 2011.

380 Babb, D. G., Landy, J. C., Barber, D. G., and Galley, R. J.: Winter Sea Ice Export From the Beaufort Sea as a Preconditioning Mechanism for Enhanced Summer Melt: A Case Study of 2016, *Journal of Geophysical Research: Oceans*, 124, 6575–6600, <https://doi.org/10.1029/2019JC015053>, 2019.

Babb, D. G., Galley, R. J., Howell, S. E. L., Landy, J. C., Stroeve, J. C., and Barber, D. G.: Increasing Multiyear Sea Ice Loss in the Beaufort Sea: A New Export Pathway for the Diminishing Multiyear Ice Cover of the Arctic Ocean, *Geophysical Research Letters*, 49, e2021GL097595–e2021GL097595, <https://doi.org/10.1029/2021GL097595>, 2022.

385 Bennetts, L. G., Bitz, C. M., Feltham, D. L., Kohout, A. L., and Meylan, M. H.: Theory, modelling and observations of marginal ice zone dynamics: multidisciplinary perspectives and outlooks, *Philosophical Transactions of the Royal Society A: Mathematical, Physical and Engineering Sciences*, 380, 20210265–20210265, <https://doi.org/10.1098/rsta.2021.0265>, 2022.

Cohanim, K., Zhao, K. X., and Stewart, A. L.: Dynamics of Eddies Generated by Sea Ice Leads, *Journal of Physical Oceanography*, 51, 3071–3092, <https://doi.org/10.1175/JPO-D-20-0169.1>, 2021.

390 Creamean, J. M., Barry, K., Hill, T. C. J., Hume, C., DeMott, P. J., Shupe, M. D., Dahlke, S., Willmes, S., Schmale, J., Beck, I., Hoppe, C. J. M., Fong, A., Chamberlain, E., Bowman, J., Scharien, R., and Persson, O.: Annual cycle observations of aerosols capable of ice formation in central Arctic clouds, *Nature Communications*, 13, 3537–3537, <https://doi.org/10.1038/s41467-022-31182-x>, 2022.

Dee, D. P., Uppala, S. M., Simmons, A. J., Berrisford, P., Poli, P., Kobayashi, S., Andrae, U., Balmaseda, M. A., Balsamo, G., Bauer, P., Bechtold, P., Beljaars, A. C. M., van de Berg, L., Bidlot, J., Bormann, N., Delsol, C., Dragani, R., Fuentes, M., Geer, A. J., Haimberger, L., Healy, S. B., Hersbach, H., Hólm, E. V., Isaksen, L., Kållberg, P., Köhler, M., Matricardi, M., McNally, A. P., Monge-Sanz, B. M., Morcrette, J.-J., Park, B.-K., Peubey, C., de Rosnay, P., Tavolato, C., Thépaut, J.-N., and Vitart, F.: The ERA-Interim reanalysis: configuration and performance of the data assimilation system, *Quarterly Journal of the Royal Meteorological Society*, 137, 553–597, <https://doi.org/https://doi.org/10.1002/qj.828>, [eprint: https://rmets.onlinelibrary.wiley.com/doi/pdf/10.1002/qj.828](https://rmets.onlinelibrary.wiley.com/doi/pdf/10.1002/qj.828), 2011.

395 Eicken, H., Shapiro, L., Heinrichs, T., Gens, R., Meyer, F., Mahoney, A., Gaylord, A., and Ak, H.: Mapping and characterization of recurring spring leads and landfast ice in the Beaufort and Chukchi Seas, 2012.

400 Feltham, D. L.: Sea Ice Rheology, *Annual Review of Fluid Mechanics*, 40, 91–112, <https://doi.org/10.1146/annurev.fluid.40.111406.102151>, 2008.

Frey, K. E., Moore, G. W. K., Cooper, L. W., and Grebmeier, J. M.: Divergent patterns of recent sea ice cover across the Bering, Chukchi, and Beaufort seas of the Pacific Arctic Region, *Progress in Oceanography*, 136, 32–49, <https://doi.org/10.1016/j.pocean.2015.05.009>, 2015.

405 Graham, R. M., Itkin, P., Meyer, A., Sundfjord, A., Spreen, G., Smedsrød, L. H., Liston, G. E., Cheng, B., Cohen, L., Divine, D., Fer, I., Fransson, A., Gerland, S., Haapala, J., Hudson, S. R., Johansson, A. M., King, J., Merkouriadi, I., Peterson, A. K., Provost, C., Randelhoff, A., Rinke, A., Rösel, A., Sennéchael, N., Walden, V. P., Duarte, P., Assmy, P., Steen, H., and Granskog, M. A.: Winter storms accelerate the demise of sea ice in the Atlantic sector of the Arctic Ocean, *Scientific Reports*, 9, 9222–9222, <https://doi.org/10.1038/s41598-019-45574-5>, 2019.

410 Gutjahr, O., Heinemann, G., Preußner, A., Willmes, S., and Drüe, C.: Quantification of ice production in Laptev Sea polynyas and its sensitivity to thin-ice parameterizations in a regional climate model, *The Cryosphere*, 10, 2999–3019, <https://doi.org/10.5194/tc-10-2999-2016>, 2016.

References

435 Aksenov, Y., Ivanov, V. V., Nurser, A. J. G., Bacon, S., Polyakov, I. V., Coward, A. C., Naveira-Garabato, A. C., and Beszczynska-Moeller, A.: The Arctic Circumpolar Boundary Current, *Journal of Geophysical Research: Oceans*, 116, <https://doi.org/10.1029/2010JC006637>, 2011.

Aue, L., Vihma, T., Uotila, P., and Rinke, A.: New Insights Into Cyclone Impacts on Sea Ice in the Atlantic Sector of the Arctic Ocean in Winter, *Geophysical Research Letters*, 49, e2022GL100051, [https://doi.org/https://doi.org/10.1029/2022GL100051](https://doi.org/10.1029/2022GL100051), 2022.

440 Babb, D. G., Landy, J. C., Barber, D. G., and Galley, R. J.: Winter Sea Ice Export From the Beaufort Sea as a Preconditioning Mechanism for Enhanced Summer Melt: A Case Study of 2016, *Journal of Geophysical Research: Oceans*, 124, 6575–6600, <https://doi.org/10.1029/2019JC015053>, 2019.

Babb, D. G., Galley, R. J., Howell, S. E. L., Landy, J. C., Stroeve, J. C., and Barber, D. G.: Increasing Multiyear Sea Ice Loss in the Beaufort Sea: A New Export Pathway for the Diminishing Multiyear Ice Cover of the Arctic Ocean, *Geophysical Research Letters*, 49, e2021GL097595–e2021GL097595, <https://doi.org/10.1029/2021GL097595>, 2022.

445 Bennetts, L. G., Bitz, C. M., Feltham, D. L., Kohout, A. L., and Meylan, M. H.: Theory, modelling and observations of marginal ice zone dynamics: multidisciplinary perspectives and outlooks, *Philosophical Transactions of the Royal Society A: Mathematical, Physical and Engineering Sciences*, 380, 20210265–20210265, <https://doi.org/10.1098/rsta.2021.0265>, 2022.

Cohanim, K., Zhao, K. X., and Stewart, A. L.: Dynamics of Eddies Generated by Sea Ice Leads, *Journal of Physical Oceanography*, 51, 450 3071–3092, <https://doi.org/10.1175/JPO-D-20-0169.1>, 2021.

Creamean, J. M., Barry, K., Hill, T. C. J., Hume, C., DeMott, P. J., Shupe, M. D., Dahlke, S., Willmes, S., Schmale, J., Beck, I., Hoppe, C. J. M., Fong, A., Chamberlain, E., Bowman, J., Scharien, R., and Persson, O.: Annual cycle observations of aerosols capable of ice formation in central Arctic clouds, *Nature Communications*, 13, 3537–3537, <https://doi.org/10.1038/s41467-022-31182-x>, 2022.

455 Dee, D. P., Uppala, S. M., Simmons, A. J., Berrisford, P., Poli, P., Kobayashi, S., Andrae, U., Balmaseda, M. A., Balsamo, G., Bauer, P., Bechtold, P., Beljaars, A. C. M., van de Berg, L., Bidlot, J., Bormann, N., Delsol, C., Dragani, R., Fuentes, M., Geer, A. J., Haimberger, L., Healy, S. B., Hersbach, H., Hólm, E. V., Isaksen, L., Källberg, P., Köhler, M., Matricardi, M., McNally, A. P., Monge-Sanz, B. M., Morcrette, J.-J., Park, B.-K., Peubey, C., de Rosnay, P., Tavolato, C., Thépaut, J.-N., and Vitart, F.: The ERA-Interim reanalysis: configuration and performance of the data assimilation system, *Quarterly Journal of the Royal Meteorological Society*, 137, 553–597, <https://doi.org/https://doi.org/10.1002/qj.828>, 2011.

460 Eicken, H., Shapiro, L., Heinrichs, T., Gens, R., Meyer, F., Mahoney, A., Gaylord, A., and Ak, H.: Mapping and characterization of recurring spring leads and landfast ice in the Beaufort and Chukchi Seas, 2012.

Feltham, D. L.: Sea Ice Rheology, *Annual Review of Fluid Mechanics*, 40, 91–112, <https://doi.org/10.1146/annurev.fluid.40.111406.102151>, 2008.

Frey, K. E., Moore, G. W. K., Cooper, L. W., and Grebmeier, J. M.: Divergent patterns of recent sea ice cover across the Bering, Chukchi, and 465 Beaufort seas of the Pacific Arctic Region, *Progress in Oceanography*, 136, 32–49, <https://doi.org/10.1016/j.pocean.2015.05.009>, 2015.

Graham, R. M., Itkin, P., Meyer, A., Sundfjord, A., Spreen, G., Smedsrød, L. H., Liston, G. E., Cheng, B., Cohen, L., Divine, D., Fer, I., Fransson, A., Gerland, S., Haapala, J., Hudson, S. R., Johansson, A. M., King, J., Merkouriadi, I., Peterson, A. K., Provost, C., Randelhoff, A., Rinke, A., Rösel, A., Sennéchael, N., Walden, V. P., Duarte, P., Assmy, P., Steen, H., and Granskog, M. A.: Winter storms accelerate

Harms, I. H. and Karcher, M. J.: Kara Sea freshwater dispersion and export in the late 1990s, *Journal of Geophysical Research: Oceans*, 110, <https://doi.org/10.1029/2004JC002744>, 2005.

415 Hartmann, M., Adachi, K., Eppers, O., Haas, C., Herber, A., Holzinger, R., Hünerbein, A., Jäkel, E., Jentzsch, C., van Pinx-teren, M., Wex, H., Willmes, S., and Stratmann, F.: Wintertime Airborne Measurements of Ice Nucleating Particles in the High Arctic: A Hint to a Marine, Biogenic Source for Ice Nucleating Particles, *Geophysical Research Letters*, 47, e2020GL087770, <https://doi.org/https://doi.org/10.1029/2020GL087770>, _eprint: <https://agupubs.onlinelibrary.wiley.com/doi/pdf/10.1029/2020GL087770>, 2020.

Hegyi, B. M. and Taylor, P. C.: The regional influence of the Arctic Oscillation and Arctic Dipole on the wintertime Arctic surface radiation budget and sea ice growth, *Geophys. Res. Lett.*, 44, 4341–4350–4341–4350, <https://doi.org/10.1002/2017GL073281>, 2017.

Heinemann, G., Willmes, S., Schefczyk, L., Makshtas, A., Kustov, V., and Makhotina, I.: Observations and Simulations of Meteorological Conditions over Arctic Thick Sea Ice in Late Winter during the Transarktika 2019 Expedition, *Atmosphere*, 12, <https://doi.org/10.3390/atmos12020174>, 2021.

Heinemann, G., Schefczyk, L., Willmes, S., and Shupe, M. D.: Evaluation of simulations of near-surface variables using the regional climate model CCLM for the MOSAiC winter period, *Elementa: Science of the Anthropocene*, 10, <https://doi.org/10.1525/elementa.2022.00033>, 2022.

Hersbach, H., Bell, B., Berrisford, P., Hirahara, S., Horányi, A., Muñoz-Sabater, J., Nicolas, J., Peubey, C., Radu, R., Schepers, D., Simmons, A., Soci, C., Abdalla, S., Abellán, X., Balsamo, G., Bechtold, P., Biavati, G., Bidlot, J., Bonavita, M., De Chiara, G., Dahlgren, P., Dee, D., Díamantakis, M., Dragani, R., Flemming, J., Forbes, R., Fuentes, M., Geer, A., Haimberger, L., Healy, S., Hogan, R. J., 430 Hólm, E., Janisková, M., Keeley, S., Laloyaux, P., Lopez, P., Lupu, C., Radnoti, G., de Rosnay, P., Rozum, I., Vamborg, F., Villaloume, S., and Thépaut, J.-N.: The ERA5 global reanalysis, *Quarterly Journal of the Royal Meteorological Society*, 146, 1999–2049, <https://doi.org/10.1002/qj.3803>, 2020.

Hoffman, J. P., Ackerman, S. A., Liu, Y., and Key, J. R.: A 20-Year Climatology of Sea Ice Leads Detected in Infrared Satellite Imagery Using a Convolutional Neural Network, *Remote Sensing*, 14, <https://doi.org/10.3390/rs14225763>, 2022.

435 Holloway, G. and Proshutinsky, A.: Role of tides in Arctic ocean/ice climate, *Journal of Geophysical Research: Oceans*, 112, <https://doi.org/10.1029/2006JC003643>, 2007.

Hutchings, J. K. and Rigor, I. G.: Role of ice dynamics in anomalous ice conditions in the Beaufort Sea during 2006 and 2007, *Journal of Geophysical Research: Oceans*, 117, <https://doi.org/10.1029/2011JC007182>, 2012.

Hwang, B., Wilkinson, J., Maksym, T., Gruber, H. C., Schweiger, A., Horvat, C., Perovich, D. K., Arntsen, A. E., Stanton, T. P., Ren, J., and 440 Wadhams, P.: Winter-to-summer transition of Arctic sea ice breakup and floe size distribution in the Beaufort Sea, *Elementa: Science of the Anthropocene*, 5, <https://doi.org/10.1525/elementa.232>, 2017.

Jakobsson, M., Mayer, L. A., Bringensparr, C., Castro, C. F., Mohammad, R., Johnson, P., Ketter, T., Accettella, D., Amblas, D., An, L., Arndt, J. E., Canals, M., Casamor, J. L., Chauché, N., Coakley, B., Danielson, S., Demarte, M., Dickson, M.-L., Dorschel, B., Dowdeswell, J. A., Dreutter, S., Fremand, A. C., Gallant, D., Hall, J. K., Hehemann, L., Hodnesdal, H., Hong, J., Ivaldi, R., Kane, E., Klaucke, I., Krawczyk, 445 D. W., Kristoffersen, Y., Kuipers, B. R., Millan, R., Masetti, G., Morlighem, M., Noormets, R., Prescott, M. M., Rebesco, M., Rignot, E., Semiletov, I., Tate, A. J., Travaglini, P., Velicogna, I., Weatherall, P., Weinrebe, W., Willis, J. K., Wood, M., Zarayskaya, Y., Zhang, T., Zimmermann, M., and Zinglersen, K. B.: The International Bathymetric Chart of the Arctic Ocean Version 4.0, *Scientific Data*, 7, 176–176, <https://doi.org/10.1038/s41597-020-0520-9>, 2020.

the demise of sea ice in the Atlantic sector of the Arctic Ocean, *Scientific Reports*, 9, 9222, <https://doi.org/10.1038/s41598-019-45574-5>, 2019.

470

Gutjahr, O., Heinemann, G., Preußen, A., Willmes, S., and Drüe, C.: Quantification of ice production in Laptev Sea polynyas and its sensitivity to thin-ice parameterizations in a regional climate model, *The Cryosphere*, 10, 2999–3019, <https://doi.org/10.5194/tc-10-2999-2016>, 2016.

Harms, I. H. and Kärcher, M. J.: Kara Sea freshwater dispersion and export in the late 1990s, *Journal of Geophysical Research: Oceans*, 110, <https://doi.org/10.1029/2004JC002744>, 2005.

475

Hegyi, B. M. and Taylor, P. C.: The regional influence of the Arctic Oscillation and Arctic Dipole on the wintertime Arctic surface radiation budget and sea ice growth, *Geophys. Res. Lett.*, 44, 4341–4350–4341–4350, <https://doi.org/10.1002/2017GL073281>, 2017.

Heinemann, G., Willmes, S., Schefczyk, L., Makshtas, A., Kustov, V., and Makhotina, I.: Observations and Simulations of Meteorological Conditions over Arctic Thick Sea Ice in Late Winter during the Transarktika 2019 Expedition, *Atmosphere*, 12, <https://doi.org/10.3390/atmos12020174>, 2021.

480

Heinemann, G., Schefczyk, L., Willmes, S., and Shupe, M. D.: Evaluation of simulations of near-surface variables using the regional climate model CCLM for the MOSAiC winter period, *Elementa: Science of the Anthropocene*, 10, <https://doi.org/10.1525/elementa.2022.00033>, 2022.

Hersbach, H., Bell, B., Berrisford, P., Hirahara, S., Horányi, A., Muñoz-Sabater, J., Nicolas, J., Peubey, C., Radu, R., Schepers, D., Simmons, A., Soci, C., Abdalla, S., Abellán, X., Balsamo, G., Bechtold, P., Biavati, G., Bidlot, J., Bonavita, M., De Chiara, G., Dahlgren, P., Dee, D., Diamantakis, M., Dragani, R., Flemming, J., Forbes, R., Fuentes, M., Geer, A., Haimberger, L., Healy, S., Hogan, R. J., Hölm, E., Janisková, M., Keeley, S., Laloyaux, P., Lopez, P., Lupu, C., Radnoti, G., de Rosnay, P., Rozum, I., Vamborg, F., Vil-laume, S., and Thépaut, J.-N.: The ERA5 global reanalysis, *Quarterly Journal of the Royal Meteorological Society*, 146, 1999–2049, <https://doi.org/10.1002/qj.3803>, 2020.

Hoffman, J. P., Ackerman, S. A., Liu, Y., and Key, J. R.: A 20-Year Climatology of Sea Ice Leads Detected in Infrared Satellite Imagery 490 Using a Convolutional Neural Network, *Remote Sensing*, 14, <https://doi.org/10.3390/rs14225763>, 2022.

Holloway, G. and Proshutinsky, A.: Role of tides in Arctic ocean/ice climate, *Journal of Geophysical Research: Oceans*, 112, <https://doi.org/10.1029/2006JC003643>, 2007.

Hutchings, J. K. and Rigor, I. G.: Role of ice dynamics in anomalous ice conditions in the Beaufort Sea during 2006 and 2007, *Journal of Geophysical Research: Oceans*, 117, <https://doi.org/10.1029/2011JC007182>, 2012.

495

Hwang, B., Wilkinson, J., Maksym, T., Gruber, H. C., Schweiger, A., Horvat, C., Perovich, D. K., Arntsen, A. E., Stanton, T. P., Ren, J., and Wadhams, P.: Winter-to-summer transition of Arctic sea ice breakup and floe size distribution in the Beaufort Sea, *Elementa: Science of the Anthropocene*, 5, <https://doi.org/10.1525/elementa.232>, 2017.

Jakobsson, M., Mayer, L. A., Bringensparr, C., Castro, C. F., Mohammad, R., Johnson, P., Ketter, T., Accettella, D., Amblas, D., An, L., Arndt, J. E., Canals, M., Casamor, J. L., Chauché, N., Coakley, B., Danielson, S., Demarte, M., Dickson, M.-L., Dorschel, B., Dowdeswell, J. A., Dreutter, S., Fremand, A. C., Gallant, D., Hall, J. K., Hehemann, L., Hodnesdal, H., Hong, J., Ivaldi, R., Kane, E., Klaucke, I., Krawczyk, D. W., Kristoffersen, Y., Kuipers, B. R., Millan, R., Masetti, G., Morlighem, M., Noormets, R., Prescott, M. M., Rebesco, M., Rignot, E., Semiletov, I., Tate, A. J., Travaglini, P., Velicogna, I., Weatherall, P., Weinrebe, W., Willis, J. K., Wood, M., Zarayskaya, Y., Zhang, T., Zimmermann, M., and Zinglersen, K. B.: The International Bathymetric Chart of the Arctic Ocean Version 4.0, *Scientific Data*, 7, 176–176, <https://doi.org/10.1038/s41597-020-0520-9>, 2020.

505

Janout, M. A. and Lenn, Y.-D.: Semidiurnal Tides on the Laptev Sea Shelf with Implications for Shear and Vertical Mixing, *Journal of Physical Oceanography*, 44, 202–219, <https://doi.org/10.1175/JPO-D-12-0240.1>, 2014.

Janout, M. A. and Lenn, Y.-D.: Semidiurnal Tides on the Laptev Sea Shelf with Implications for Shear and Vertical Mixing, *Journal of Physical Oceanography*, 44, 202–219, <https://doi.org/10.1175/JPO-D-12-0240.1>, 2014.

450 Janout, M. A., Aksenov, Y., Hölemann, J. A., Rabe, B., Schauer, U., Polyakov, I. V., Bacon, S., Coward, A. C., Karcher, M., Lenn, Y.-D., Kassens, H., and Timokhov, L.: Kara Sea freshwater transport through Vilkitsky Strait: Variability, forcing, and further pathways toward the western Arctic Ocean from a model and observations, *Journal of Geophysical Research: Oceans*, 120, 4925–4944, <https://doi.org/10.1002/2014JC010635>, 2015.

455 Janout, M. A., Hölemann, J., Laukert, G., Smirnov, A., Krumpen, T., Bauch, D., and Timokhov, L.: On the Variability of Stratification in the Freshwater-Influenced Laptev Sea Region, *Frontiers in Marine Science*, 7, <https://doi.org/10.3389/fmars.2020.543489>, 2020.

Kirchmeier-Young, M. C., Zwiers, F. W., and Gillett, N. P.: Attribution of Extreme Events in Arctic Sea Ice Extent, *Journal of Climate*, 30, 553–571, <https://doi.org/10.1175/JCLI-D-16-0412.1>, 2017.

460 Kohnemann, S. and Heinemann, G.: A climatology of wintertime low-level jets in Nares Strait, *Polar Research*, 40, <https://doi.org/10.33265/polar.v40.3622>, 2021.

Korosov, A., Rampal, P., Ying, Y., Ólason, E., and Williams, T.: Towards improving short-term sea ice predictability using deformation observations, *The Cryosphere Discussions*, 2022, 1–20–1–20, <https://doi.org/10.5194/tc-2022-46>, 2022.

Kort, E. A., Wofsy, S. C., Daube, B. C., Diao, M., Elkins, J. W., Gao, R. S., Hintsa, E. J., Hurst, D. F., Jimenez, R., Moore, F. L., Spackman, J. R., and Zondlo, M. A.: Atmospheric observations of Arctic Ocean methane emissions up to 82° north, *Nature Geoscience*, 5, 318–321–318–321, <https://doi.org/10.1038/ngeo1452>, 2012.

465 Kwok, R., Spreen, G., and Pang, S.: Arctic sea ice circulation and drift speed: Decadal trends and ocean currents, *Journal of Geophysical Research: Oceans*, 118, 2408–2425, <https://doi.org/10.1002/jgrc.20191>, 2013.

Levitus, S., Locarnini, R. A., Boyer, T. P., Mishonov, A. V., Antonov, J. I., Garcia, H. E., Baranova, O. K., Zweng, M. M., Johnson, D. R., and Seidov, 1948, D.: World ocean atlas 2009, <https://repository.library.noaa.gov/view/noaa/1259>, 2010.

470 Liu, Z., Risi, C., Codron, F., Jian, Z., Wei, Z., He, X., Poulsen, C. J., Wang, Y., Chen, D., Ma, W., Cheng, Y., and Bowen, G. J.: Atmospheric forcing dominates winter Barents-Kara sea ice variability on interannual to decadal time scales, *Proceedings of the National Academy of Sciences*, 119, e2120770 119–e2120770 119, <https://doi.org/10.1073/pnas.2120770119>, 2022.

Lüpkes, C., Vihma, T., Birnbaum, G., and Wacker, U.: Influence of leads in sea ice on the temperature of the atmospheric boundary layer during polar night, *Geophysical Research Letters*, 35, <https://doi.org/10.1029/2007GL032461>, 2008.

475 Manucharyan, G. E. and Thompson, A. F.: Heavy footprints of upper-ocean eddies on weakened Arctic sea ice in marginal ice zones, *Nature Communications*, 13, 2147–2147, <https://doi.org/10.1038/s41467-022-29663-0>, 2022.

Marcq, S. and Weiss, J.: Influence of sea ice lead-width distribution on turbulent heat transfer between the ocean and the atmosphere, *The Cryosphere*, 6, 143–156–143–156, <https://doi.org/10.5194/tc-6-143-2012>, 2012.

Mioduszewski, J., Vavrus, S., and Wang, M.: Diminishing Arctic Sea Ice Promotes Stronger Surface Winds, *Journal of Climate*, 31, 8101–8119, <https://doi.org/10.1175/JCLI-D-18-0109.1>, 2018.

480 Moore, C. W., Obrist, D., Steffen, A., Staebler, R. M., Douglas, T. A., Richter, A., and Nghiem, S. V.: Convective forcing of mercury and ozone in the Arctic boundary layer induced by leads in sea ice, *Nature*, 506, 81–84–81–84, <https://doi.org/10.1038/nature12924>, 2014.

Nguyen, A. T., Menemenlis, D., and Kwok, R.: Improved modeling of the Arctic halocline with a subgrid-scale brine rejection parameterization, *Journal of Geophysical Research: Oceans*, 114, <https://doi.org/10.1029/2008JC005121>, 2009.

485 Notz, D. and Community, S. I. M. I. P.: Arctic Sea Ice in CMIP6, *Geophysical Research Letters*, 47, e2019GL086749–e2019GL086749, <https://doi.org/10.1029/2019GL086749>, 2020.

Janout, M. A., Aksenov, Y., Hölemann, J. A., Rabe, B., Schauer, U., Polyakov, I. V., Bacon, S., Coward, A. C., Karcher, M., Lenn, Y.-D., Kassens, H., and Timokhov, L.: Kara Sea freshwater transport through Vilkitsky Strait: Variability, forcing, and further pathways toward the western Arctic Ocean from a model and observations, *Journal of Geophysical Research: Oceans*, 120, 4925–4944, 510 <https://doi.org/10.1002/2014JC010635>, 2015.

Janout, M. A., Hölemann, J., Laukert, G., Smirnov, A., Krumpen, T., Bauch, D., and Timokhov, L.: On the Variability of Stratification in the Freshwater-Influenced Laptev Sea Region, *Frontiers in Marine Science*, 7, <https://doi.org/10.3389/fmars.2020.543489>, 2020.

Jewell, M. E. and Hutchings, J. K.: Observational Perspectives on Beaufort Sea Ice Breakouts, *Geophysical Research Letters*, 50, e2022GL101 408, <https://doi.org/https://doi.org/10.1029/2022GL101408>, 2023.

515 Jewell, M. E., Hutchings, J. K., and Geiger, C. A.: Atmospheric highs drive asymmetric sea ice drift during lead opening from Point Barrow, *The Cryosphere Discussions*, 2023, 1–33, <https://doi.org/10.5194/tc-2023-9>, 2023.

Kirchmeier-Young, M. C., Zwiers, F. W., and Gillett, N. P.: Attribution of Extreme Events in Arctic Sea Ice Extent, *Journal of Climate*, 30, 553–571, <https://doi.org/10.1175/JCLI-D-16-0412.1>, 2017.

Kohnemann, S. and Heinemann, G.: A climatology of wintertime low-level jets in Nares Strait, *Polar Research*, 40, 520 <https://doi.org/10.33265/polar.v40.3622>, 2021.

Korosov, A., Rampal, P., Ying, Y., Ólason, E., and Williams, T.: Towards improving short-term sea ice predictability using deformation observations, *The Cryosphere Discussions*, 2022, 1–20–1–20, <https://doi.org/10.5194/tc-2022-46>, 2022.

Kort, E. A., Wofsy, S. C., Daube, B. C., Diao, M., Elkins, J. W., Gao, R. S., Hintsa, E. J., Hurst, D. F., Jimenez, R., Moore, F. L., Spackman, J. R., and Zondlo, M. A.: Atmospheric observations of Arctic Ocean methane emissions up to 82° north, *Nature Geoscience*, 5, 318–321–525 318–321, <https://doi.org/10.1038/ngeo1452>, 2012.

Kwok, R., Spreen, G., and Pang, S.: Arctic sea ice circulation and drift speed: Decadal trends and ocean currents, *Journal of Geophysical Research: Oceans*, 118, 2408–2425, <https://doi.org/10.1002/jgrc.20191>, 2013.

Levitus, S., Locarnini, R. A., Boyer, T. P., Mishonov, A. V., Antonov, J. I., Garcia, H. E., Baranova, O. K., Zweng, M. M., Johnson, D. R., and Seidov, 1948, D.: World ocean atlas 2009, <https://repository.library.noaa.gov/view/noaa/1259>, 2010.

530 Lewis, B. J. and Hutchings, J. K.: Leads and Associated Sea Ice Drift in the Beaufort Sea in Winter, *Journal of Geophysical Research: Oceans*, 124, 3411–3427, <https://doi.org/https://doi.org/10.1029/2018JC014898>, 2019.

Liu, Z., Risi, C., Codron, F., Jian, Z., Wei, Z., He, X., Poulsen, C. J., Wang, Y., Chen, D., Ma, W., Cheng, Y., and Bowen, G. J.: Atmospheric forcing dominates winter Barents-Kara sea ice variability on interannual to decadal time scales, *Proceedings of the National Academy of Sciences*, 119, e2120770 119–e2120770 119, <https://doi.org/10.1073/pnas.2120770119>, 2022.

535 Lüpkes, C., Vihma, T., Birnbaum, G., and Wacker, U.: Influence of leads in sea ice on the temperature of the atmospheric boundary layer during polar night, *Geophysical Research Letters*, 35, <https://doi.org/10.1029/2007GL032461>, 2008.

Manucharyan, G. E. and Thompson, A. F.: Heavy footprints of upper-ocean eddies on weakened Arctic sea ice in marginal ice zones, *Nature Communications*, 13, 2147–2147, <https://doi.org/10.1038/s41467-022-29663-0>, 2022.

Marcq, S. and Weiss, J.: Influence of sea ice lead-width distribution on turbulent heat transfer between the ocean and the atmosphere, *The Cryosphere*, 6, 143–156–143–156, <https://doi.org/10.5194/tc-6-143-2012>, 2012.

540 Mioduszewski, J., Vavrus, S., and Wang, M.: Diminishing Arctic Sea Ice Promotes Stronger Surface Winds, *Journal of Climate*, 31, 8101–8119, <https://doi.org/10.1175/JCLI-D-18-0109.1>, 2018.

Moore, C. W., Obrist, D., Steffen, A., Staebler, R. M., Douglas, T. A., Richter, A., and Nghiem, S. V.: Convective forcing of mercury and ozone in the Arctic boundary layer induced by leads in sea ice, *Nature*, 506, 81–84–81–84, <https://doi.org/10.1038/nature12924>, 2014.

Park, H.-S., Lee, S., Son, S.-W., Feldstein, S. B., and Kosaka, Y.: The Impact of Poleward Moisture and Sensible Heat Flux on Arctic Winter Sea Ice Variability, *Journal of Climate*, 28, 5030–5040, <https://doi.org/10.1175/JCLI-D-15-0074.1>, 2015.

Pavlova, O., Pavlov, V., and Gerland, S.: The impact of winds and sea surface temperatures on the Barents Sea ice extent, a statistical approach, *Journal of Marine Systems*, 130, 248–255, <https://doi.org/10.1016/j.jmarsys.2013.02.011>, 2014.

Pnyushkov, A. V., Polyakov, I. V., Ivanov, V. V., Aksenov, Y., Coward, A. C., Janout, M., and Rabe, B.: Structure and variability of the boundary current in the Eurasian Basin of the Arctic Ocean, *Deep Sea Research Part I: Oceanographic Research Papers*, 101, 80–97, <https://doi.org/10.1016/j.dsr.2015.03.001>, 2015.

Polyakov, I. V., Rippeth, T. P., Fer, I., Alkire, M. B., Baumann, T. M., Carmack, E. C., Ingvaldsen, R., Ivanov, V. V., Janout, M., Lind, S., Padman, L., Pnyushkov, A. V., and Rember, R.: Weakening of Cold Halocline Layer Exposes Sea Ice to Oceanic Heat in the Eastern Arctic Ocean, *Journal of Climate*, 33, 8107–8123, <https://doi.org/10.1175/JCLI-D-19-0976.1>, 2020.

Qu, M., Pang, X., Zhao, X., Lei, R., Ji, Q., Liu, Y., and Chen, Y.: Spring leads in the Beaufort Sea and its interannual trend using Terra/MODIS thermal imagery, *Remote Sensing of Environment*, 256, 112 342–112 342, <https://doi.org/10.1016/j.rse.2021.112342>, 2021.

Reiser, F., Willmes, S., Hausmann, U., and Heinemann, G.: Predominant Sea Ice Fracture Zones Around Antarctica and Their Relation to Bathymetric Features, *Geophysical Research Letters*, 46, 12 117–12 124, <https://doi.org/10.1029/2019GL084624>, 2019.

Reiser, F., Willmes, S., and Heinemann, G.: A New Algorithm for Daily Sea Ice Lead Identification in the Arctic and Antarctic Winter from Thermal-Infrared Satellite Imagery, *Remote Sensing*, 12, 1957–1957, <https://doi.org/10.3390/rs12121957>, 2020.

Rheinländer, J. W., Davy, R., Ólason, E., Rampal, P., Spensberger, C., Williams, T. D., Korosov, A., and Spengler, T.: Driving Mechanisms of an Extreme Winter Sea Ice Breakup Event in the Beaufort Sea, *Geophysical Research Letters*, 49, e2022GL099 024–e2022GL099 024, <https://doi.org/10.1029/2022GL099024>, 2022.

Schaffer, J., Timmermann, R., Arndt, J. E., Kristensen, S. S., Mayer, C., Morlighem, M., and Steinhage, D.: A global, high-resolution data set of ice sheet topography, cavity geometry, and ocean bathymetry, *Earth System Science Data*, 8, 543–557, <https://doi.org/10.5194/essd-8-543-2016>, 2016.

Sidorenko, D., Goessling, H., Koldunov, N., Scholz, P., Danilov, S., Barbi, D., Cabos, W., Gurses, O., Harig, S., Hinrichs, C., Juricke, S., Lohmann, G., Losch, M., Mu, L., Rackow, T., Rakowsky, N., Sein, D., Semmler, T., Shi, X., Stepanek, C., Streffing, J., Wang, Q., Wekerle, C., Yang, H., and Jung, T.: Evaluation of FESOM2.0 Coupled to ECHAM6.3: Preindustrial and HighResMIP Simulations, *Journal of Advances in Modeling Earth Systems*, 11, 3794–3815, <https://doi.org/https://doi.org/10.1029/2019MS001696>, [eprint: https://agupubs.onlinelibrary.wiley.com/doi/pdf/10.1029/2019MS001696](https://agupubs.onlinelibrary.wiley.com/doi/pdf/10.1029/2019MS001696), 2019.

Smedsrød, L. H., Sirevaag, A., Kloster, K., Sorteberg, A., and Sandven, S.: Recent wind driven high sea ice area export in the Fram Strait contributes to Arctic sea ice decline, *The Cryosphere*, 5, 821–829–821–829, <https://doi.org/10.5194/tc-5-821-2011>, 2011.

Spreen, G., Kaleschke, L., and Heygster, G.: Sea ice remote sensing using AMSR-E 89-GHz channels, *Journal of Geophysical Research: Oceans*, 113, <https://doi.org/https://doi.org/10.1029/2005JC003384>, [eprint: https://agupubs.onlinelibrary.wiley.com/doi/pdf/10.1029/2005JC003384](https://agupubs.onlinelibrary.wiley.com/doi/pdf/10.1029/2005JC003384), 2008.

Spreen, G., Kwok, R., Menemenlis, D., and Nguyen, A. T.: Sea-ice deformation in a coupled ocean–sea-ice model and in satellite remote sensing data, *The Cryosphere*, 11, 1553–1573–1553–1573, <https://doi.org/10.5194/tc-11-1553-2017>, 2017.

Stabeno, P., Kachel, N., Ladd, C., and Woodgate, R.: Flow Patterns in the Eastern Chukchi Sea: 2010–2015, *Journal of Geophysical Research: Oceans*, 123, 1177–1195, <https://doi.org/10.1002/2017JC013135>, 2018.

Steger, C. and Buccignani, E.: Regional Climate Modelling with COSMO-CLM: History and Perspectives, *Atmosphere*, 11, <https://doi.org/10.3390/atmos11111250>, 2020.

545 Nguyen, A. T., Menemenlis, D., and Kwok, R.: Improved modeling of the Arctic halocline with a subgrid-scale brine rejection parameterization, *Journal of Geophysical Research: Oceans*, 114, <https://doi.org/10.1029/2008JC005121>, 2009.

Notz, D. and Community, S. I. M. I. P.: Arctic Sea Ice in CMIP6, *Geophysical Research Letters*, 47, e2019GL086749–e2019GL086749, <https://doi.org/10.1029/2019GL086749>, 2020.

Park, H.-S., Lee, S., Son, S.-W., Feldstein, S. B., and Kosaka, Y.: The Impact of Poleward Moisture and Sensible Heat Flux on Arctic Winter Sea Ice Variability, *Journal of Climate*, 28, 5030–5040, <https://doi.org/10.1175/JCLI-D-15-0074.1>, 2015.

Pavlova, O., Pavlov, V., and Gerland, S.: The impact of winds and sea surface temperatures on the Barents Sea ice extent, a statistical approach, *Journal of Marine Systems*, 130, 248–255, <https://doi.org/10.1016/j.jmarsys.2013.02.011>, 2014.

Pnyushkov, A. V., Polyakov, I. V., Ivanov, V. V., Aksenov, Y., Coward, A. C., Janout, M., and Rabe, B.: Structure and variability of the boundary current in the Eurasian Basin of the Arctic Ocean, *Deep Sea Research Part I: Oceanographic Research Papers*, 101, 80–97, <https://doi.org/10.1016/j.dsr.2015.03.001>, 2015.

Polyakov, I. V., Rippeth, T. P., Fer, I., Alkire, M. B., Baumann, T. M., Carmack, E. C., Ingvaldsen, R., Ivanov, V. V., Janout, M., Lind, S., Padman, L., Pnyushkov, A. V., and Rember, R.: Weakening of Cold Halocline Layer Exposes Sea Ice to Oceanic Heat in the Eastern Arctic Ocean, *Journal of Climate*, 33, 8107–8123, <https://doi.org/10.1175/JCLI-D-19-0976.1>, 2020.

Qu, M., Pang, X., Zhao, X., Lei, R., Ji, Q., Liu, Y., and Chen, Y.: Spring leads in the Beaufort Sea and its interannual trend using Terra/MODIS thermal imagery, *Remote Sensing of Environment*, 256, 112 342–112 342, <https://doi.org/10.1016/j.rse.2021.112342>, 2021.

550 Reiser, F., Willmes, S., Hausmann, U., and Heinemann, G.: Predominant Sea Ice Fracture Zones Around Antarctica and Their Relation to Bathymetric Features, *Geophysical Research Letters*, 46, 12 117–12 124, <https://doi.org/10.1029/2019GL084624>, 2019.

Reiser, F., Willmes, S., and Heinemann, G.: A New Algorithm for Daily Sea Ice Lead Identification in the Arctic and Antarctic Winter from Thermal-Infrared Satellite Imagery, *Remote Sensing*, 12, 1957–1957, <https://doi.org/10.3390/rs12121957>, 2020.

555 Rheinländer, J. W., Davy, R., Ólason, E., Rampal, P., Spensberger, C., Williams, T. D., Korosov, A., and Spengler, T.: Driving Mechanisms of an Extreme Winter Sea Ice Breakup Event in the Beaufort Sea, *Geophysical Research Letters*, 49, e2022GL099024–e2022GL099024, <https://doi.org/10.1029/2022GL099024>, 2022.

Schaffer, J., Timmermann, R., Arndt, J. E., Kristensen, S. S., Mayer, C., Morlighem, M., and Steinhage, D.: A global, high-resolution data set of ice sheet topography, cavity geometry, and ocean bathymetry, *Earth System Science Data*, 8, 543–557, <https://doi.org/10.5194/essd-8-543-2016>, 2016.

560 Sidorenko, D., Goessling, H., Koldunov, N., Scholz, P., Danilov, S., Barbi, D., Cabos, W., Gurses, O., Harig, S., Hinrichs, C., Juricke, S., Lohmann, G., Losch, M., Mu, L., Rackow, T., Rakowsky, N., Sein, D., Semmler, T., Shi, X., Stepanek, C., Streffing, J., Wang, Q., Wekerle, C., Yang, H., and Jung, T.: Evaluation of FESOM2.0 Coupled to ECHAM6.3: Preindustrial and HighResMIP Simulations, *Journal of Advances in Modeling Earth Systems*, 11, 3794–3815, <https://doi.org/10.1029/2019MS001696>, 2019.

565 Smedsrød, L. H., Sirevaag, A., Kloster, K., Sorteberg, A., and Sandven, S.: Recent wind driven high sea ice area export in the Fram Strait contributes to Arctic sea ice decline, *The Cryosphere*, 5, 821–829–821–829, <https://doi.org/10.5194/tc-5-821-2011>, 2011.

Spreen, G., Kaleschke, L., and Heygster, G.: Sea ice remote sensing using AMSR-E 89-GHz channels, *Journal of Geophysical Research: Oceans*, 113, <https://doi.org/10.1029/2005JC003384>, 2008.

Spreen, G., Kwok, R., Menemenlis, D., and Nguyen, A. T.: Sea-ice deformation in a coupled ocean–sea-ice model and in satellite remote sensing data, *The Cryosphere*, 11, 1553–1573–1553–1573, <https://doi.org/10.5194/tc-11-1553-2017>, 2017.

570 Stabeno, P., Kachel, N., Ladd, C., and Woodgate, R.: Flow Patterns in the Eastern Chukchi Sea: 2010–2015, *Journal of Geophysical Research: Oceans*, 123, 1177–1195, <https://doi.org/10.1002/2017JC013135>, 2018.

525 Stirling, I.: The importance of polynyas, ice edges, and leads to marine mammals and birds, *Journal of Marine Systems*, 10, 9–21, [https://doi.org/10.1016/S0924-7963\(96\)00054-1](https://doi.org/10.1016/S0924-7963(96)00054-1), 1997.

Stroeve, J. and Notz, D.: Changing state of Arctic sea ice across all seasons, *Environmental Research Letters*, 13, 103 001–103 001, <https://doi.org/10.1088/1748-9326/aade56>, 2018.

Suzuki, T., Yamazaki, D., Tsujino, H., Komuro, Y., Nakano, H., and Urakawa, S.: A dataset of continental river discharge based on JRA-55 530 for use in a global ocean circulation model, *Journal of Oceanography*, 74, 421–429, <https://doi.org/10.1007/s10872-017-0458-5>, 2018.

Wang, Q., Danilov, S., Sidorenko, D., Timmermann, R., Wekerle, C., Wang, X., Jung, T., and Schröter, J.: The Finite Element Sea Ice-Ocean Model (FESOM) v1.4: formulation of an ocean general circulation model, *Geoscientific Model Development*, 7, 663–693, <https://doi.org/10.5194/gmd-7-663-2014>, 2014.

Wang, Q., Danilov, S., Jung, T., Kaleschke, L., and Wernecke, A.: Sea ice leads in the Arctic Ocean: Model assessment, interannual variability 535 and trends, *Geophysical Research Letters*, 43, 7019–7027, <https://doi.org/10.1002/2016GL068696>, 2016.

Warner, J. L., Screen, J. A., and Scaife, A. A.: Links Between Barents-Kara Sea Ice and the Extratropical Atmospheric Circulation Explained by Internal Variability and Tropical Forcing, *Geophysical Research Letters*, 47, e2019GL085 679–e2019GL085 679, <https://doi.org/10.1029/2019GL085679>, 2020.

Wekerle, C., Wang, Q., von Appen, W.-J., Danilov, S., Schourup-Kristensen, V., and Jung, T.: Eddy-Resolving Simulation of the Atlantic 540 Water Circulation in the Fram Strait With Focus on the Seasonal Cycle, *Journal of Geophysical Research: Oceans*, 122, 8385–8405, <https://doi.org/https://doi.org/10.1002/2017JC012974>, _eprint: <https://agupubs.onlinelibrary.wiley.com/doi/pdf/10.1002/2017JC012974>, 2017.

Willmes, S. and Heinemann, G.: Pan-Arctic lead detection from MODIS thermal infrared imagery, *Annals of Glaciology*, 56, 29–37–29–37, <https://doi.org/10.3189/2015AoG69A615>, 2015.

545 Willmes, S. and Heinemann, G.: Sea-Ice Wintertime Lead Frequencies and Regional Characteristics in the Arctic, 2003–2015, *Remote Sensing*, 8, <https://doi.org/10.3390/rs8010004>, 2016.

Winsor, P. and Chapman, D. C.: Pathways of Pacific water across the Chukchi Sea: A numerical model study, *Journal of Geophysical Research: Oceans*, 109, <https://doi.org/10.1029/2003JC001962>, 2004.

Woods, C. and Caballero, R.: The Role of Moist Intrusions in Winter Arctic Warming and Sea Ice Decline, *Journal of Climate*, 29, 4473– 550 4485, <https://doi.org/10.1175/JCLI-D-15-0773.1>, 2016.

Zhang, J. and Rothrock, D. A.: Modeling Global Sea Ice with a Thickness and Enthalpy Distribution Model in Generalized Curvilinear Coordinates, *Monthly Weather Review*, 131, 845 – 861, [https://doi.org/10.1175/1520-0493\(2003\)131<0845:MGSIWA>2.0.CO;2](https://doi.org/10.1175/1520-0493(2003)131<0845:MGSIWA>2.0.CO;2), place: Boston MA, USA Publisher: American Meteorological Society, 2003.

Zhang, J., Lindsay, R., Schweiger, A., and Rigor, I.: Recent changes in the dynamic properties of declining Arctic sea ice: A model study, *Geophysical Research Letters*, 39, <https://doi.org/10.1029/2012GL053545>, 2012.

Zhang, Y., Cheng, X., Liu, J., and Hui, F.: The potential of sea ice leads as a predictor for summer Arctic sea ice extent, *The Cryosphere*, 12, 3747–3757–3747–3757, <https://doi.org/10.5194/tc-12-3747-2018>, 2018.

Årthun, M., Eldevik, T., and Smedsrød, L. H.: The Role of Atlantic Heat Transport in Future Arctic Winter Sea Ice Loss, *Journal of Climate*, 32, 3327–3341, <https://doi.org/10.1175/JCLI-D-18-0750.1>, 2019.

Steger, C. and Buccignani, E.: Regional Climate Modelling with COSMO-CLM: History and Perspectives, *Atmosphere*, 11, <https://doi.org/10.3390/atmos11111250>, 2020.

585 Stirling, I.: The importance of polynyas, ice edges, and leads to marine mammals and birds, *Journal of Marine Systems*, 10, 9–21, [https://doi.org/10.1016/S0924-7963\(96\)00054-1](https://doi.org/10.1016/S0924-7963(96)00054-1), 1997.

Stroeve, J. and Notz, D.: Changing state of Arctic sea ice across all seasons, *Environmental Research Letters*, 13, 103 001–103 001, <https://doi.org/10.1088/1748-9326/aade56>, 2018.

590 Suzuki, T., Yamazaki, D., Tsujino, H., Komuro, Y., Nakano, H., and Urakawa, S.: A dataset of continental river discharge based on JRA-55 for use in a global ocean circulation model, *Journal of Oceanography*, 74, 421–429, <https://doi.org/10.1007/s10872-017-0458-5>, 2018.

Wang, Q., Danilov, S., Sidorenko, D., Timmermann, R., Wekerle, C., Wang, X., Jung, T., and Schröter, J.: The Finite Element Sea Ice-Ocean Model (FESOM) v1.4: formulation of an ocean general circulation model, *Geoscientific Model Development*, 7, 663–693, <https://doi.org/10.5194/gmd-7-663-2014>, 2014.

595 Wang, Q., Danilov, S., Jung, T., Kaleschke, L., and Wernecke, A.: Sea ice leads in the Arctic Ocean: Model assessment, interannual variability and trends, *Geophysical Research Letters*, 43, 7019–7027, <https://doi.org/10.1002/2016GL068696>, 2016.

Warner, J. L., Screen, J. A., and Scaife, A. A.: Links Between Barents-Kara Sea Ice and the Extratropical Atmospheric Circulation Explained by Internal Variability and Tropical Forcing, *Geophysical Research Letters*, 47, e2019GL085 679–e2019GL085 679, <https://doi.org/10.1029/2019GL085679>, 2020.

600 Wekerle, C., Wang, Q., von Appen, W.-J., Danilov, S., Schourup-Kristensen, V., and Jung, T.: Eddy-Resolving Simulation of the Atlantic Water Circulation in the Fram Strait With Focus on the Seasonal Cycle, *Journal of Geophysical Research: Oceans*, 122, 8385–8405, <https://doi.org/https://doi.org/10.1002/2017JC012974>, _eprint: <https://agupubs.onlinelibrary.wiley.com/doi/pdf/10.1002/2017JC012974>, 2017.

Willmes, S. and Heinemann, G.: Pan-Arctic lead detection from MODIS thermal infrared imagery, *Annals of Glaciology*, 56, 29–37–29–37, <https://doi.org/10.3189/2015AoG69A615>, 2015.

605 Willmes, S. and Heinemann, G.: Sea-Ice Wintertime Lead Frequencies and Regional Characteristics in the Arctic, 2003–2015, *Remote Sensing*, 8, <https://doi.org/10.3390/rs8010004>, 2016.

Winsor, P. and Chapman, D. C.: Pathways of Pacific water across the Chukchi Sea: A numerical model study, *Journal of Geophysical Research: Oceans*, 109, <https://doi.org/10.1029/2003JC001962>, 2004.

610 Woods, C. and Caballero, R.: The Role of Moist Intrusions in Winter Arctic Warming and Sea Ice Decline, *Journal of Climate*, 29, 4473–4485, <https://doi.org/10.1175/JCLI-D-15-0773.1>, 2016.

Zhang, J. and Rothrock, D. A.: Modeling Global Sea Ice with a Thickness and Enthalpy Distribution Model in Generalized Curvilinear Coordinates, *Monthly Weather Review*, 131, 845 – 861, [https://doi.org/10.1175/1520-0493\(2003\)131<0845:MGSIWA>2.0.CO;2](https://doi.org/10.1175/1520-0493(2003)131<0845:MGSIWA>2.0.CO;2), place: Boston MA, USA Publisher: American Meteorological Society, 2003.

615 Zhang, J., Lindsay, R., Schweiger, A., and Rigor, I.: Recent changes in the dynamic properties of declining Arctic sea ice: A model study, *Geophysical Research Letters*, 39, <https://doi.org/10.1029/2012GL053545>, 2012.

Zhang, Y., Cheng, X., Liu, J., and Hui, F.: The potential of sea ice leads as a predictor for summer Arctic sea ice extent, *The Cryosphere*, 12, 3747–3757–3747–3757, <https://doi.org/10.5194/tc-12-3747-2018>, 2018.

Årthun, M., Eldevik, T., and Smedsrød, L. H.: The Role of Atlantic Heat Transport in Future Arctic Winter Sea Ice Loss, *Journal of Climate*, 32, 3327–3341, <https://doi.org/10.1175/JCLI-D-18-0750.1>, 2019.